Supporting Information

Luminescent Dinuclear Ruthenium Terpyridine Complexes with a Bis-Phenylbenzimidazole Spacer

Debiprasad Mondal, Sourav Biswas, Animesh Paul, and Sujoy Baitalik*

Department of Chemistry, Inorganic Chemistry Section, Jadavpur University,
Kolkata –700032, India

Physical Measurements. Vario-Micro V2.0.11 elemental (CHNSO) analyzer was used to analyze the C, H, and N content in the compounds. ESI mass spectra were recorded on a Waters Xevo G2 QTOf mass spectrometer. NMR spectra of the compounds were acquired on either a Bruker 300 or Bruker 500 spectrometer. Shimadzu UV 1800 spectrometer and Horiba Fluoromax-4 spectroflurometer were used to acquire UV-vis absorption and steady state luminescence spectra, respectively. Quantum yields of the compounds were estimated by taking $[Ru(bpy)_3]^{2+}$ as the reference. Lifetimes of the compounds were measured by using time-correlated single photon counting set up from Horiba Jobin-Yvon. The luminescence decay data were collected on a Hamamatsu MCP photomultiplier (R3809) and were analyzed by using IBH DAS6 software.

Cyclic and square wave voltammograms of the complexes were recorded via a BAS epsilon electrochemistry system. Three-electrode assembly comprising of a platinum or glassy carbon working electrode, a platinum counter electrode, and Ag/AgCl reference electrode was used for the study. Tetraethyl ammonium perchlorate (TEAP) was used as background electrolyte in all the electrochemical experiments. The potentials of the complexes are reported with respect to Ag/AgCl reference electrode, which under the identical experimental conditions gave a value of 0.36 V for the Fc/Fc^+ couple.

Theoretical Computational Methods. Quantum chemical calculations were performed with the Gaussian 09 program[S1] employing the DFT method with Becke's three-parameter hybrid functional and Lee-Yang-Parr's gradient corrected correlation functional B3LYP level of theory.[S2-S3] The 6-31G(d) basis set was employed for the C, H, N, and O while SDD basis set was used for Ru atom. [S4] Geometries were fully optimized using the criteria of the respective programs. TD-DFT[S5-S8] calculations of the singlet-singlet excitations were performed in acetonitrile simulated by the CPCM model [S9] by using the so-called nonequilibrium approach, which has been designed for the study of the absorption process.[S10-S11] We also perform the UKS calculations directly on the triplet state of the complexes to calculate singlet-triplet energy gap. Orbital analysis was completed with Gauss View[S12] and Gauss sum 2.2.[S13]

Optimization of hydrogen-bonded adduct of complex 1 and 3. Firstly, we optimized the geometry by incorpaorating four DMSO molecules in the vicinity of four imidazole proton attached to H_2pbbzim terminal ligands, while in the second case, we optimized the geometry by incorporating six DMSO molecules in the vicinity of all the six imidazole NH protons in the

complex. The final optimized geometry in first case is ended up with hydrogen-bonded adduct where two opposite NH protons form strong NH-----O hydrogen bond with a distance of 1.69 Å (Figure S23, SI), while the remaining two NH protons form almost equally strong NH-----O hydrogen bonds with a distance of 1.71 Å. In the second category, six DMSO molecules were found to be intermolecularly hydrogen bonded with six NH protons in **3** and three types of NH-----O distances were observed (of 1.69 Å, 1.71 Å, and of 1.77 Å) (Figure S24, SI). In case of **1**, the NH protons on the bridge form two hydrogen-bonded adduct with a NH-----O distance of 1.79 Å (Figure S25, SI). Thus, the extent of hydrogen bonding is much more with the NH protons on H_2pbbzim ligands compared with the bridging unit. The more acidic nature of NH of H_2pbbzim is also been reflected in the experimental absorption spectral red-shift in DMSO compared with acetonitrile. TD-DFT calculations of the hydrogen bonded adduct of **1** lead to the calculated absorption band at 498 nm (due to both MLCT and ILCT transitions), while the non-hydrogen bonded form of **1** yields the peak position at 484 nm. In case with **3**, hydrogen bonded adduct gives rise to the absorption band at 497 nm (due to both MLCT and ILCT transitions), while the non-hydrogen bonded form yields the peak position at 481 nm. The experimentally observed peak at 499 nm for **1** and at 502 nm for **3** in DMSO is thus correlated well with calculated results considering the hydrogen bonding interaction. Moreover, the experimentally observed solvatochromic shift for the lowest energy spin-forbidden band in **3** (830 cm^{-1}) compared with **1** (216 cm^{-1}) can also be explained by taking into consideration the stronger hydrogen bonding ability of **3**.

Anion sensing experiments. For a typical absorption and emission titration experiment, aliquots of TBA salts of F^-, CN^-, AcO^- and $H_2PO_4^-$ (5.0×10^{-3} M) were added incrementally to a 2.5 mL solution of the complexes (2.0×10^{-5} M). In aqueous medium, the experiments were carried out in H_2O:DMSO (100:1 v/v) mixture and the concentration of the metal complexes were 2×10^{-5} M. The equilibrium constants were evaluated from the absorbance data using equation (S1)[S14].

$$A_{obs} = (A_0 + A_\infty K[G]_T)/(1+ K[G]_T) \qquad \text{(S1)}$$

where A_{obs} is the observed absorbance, A_0 is the absorbance of the free receptor, A_∞ is the maximum absorbance induced by the presence of a given anionic guest, $[G]_T$ is the total concentration of the guest, and K is the equilibrium constant of the host-guest entity. Binding

constants were performed in duplicate, and the average value is reported. The lifetimes of the receptors were recorded as a function of different anions.

Sensing Behaviors in Organic Medium. The absorption and luminescence spectra of the complexes in presence of studied anions are presented in Figure S34 (SI). Among the studied anions, F^- and CN^- lead to decrease the intensity of the absorption band at 499 nm for **1** and 500 nm for **2** with concomitant evolution of broad shoulder in the range of 568-606 nm (Figure S34, SI). The extent of change is comparatively less with AcO^- in both cases. For **3**, on the other hand, dramatic red-shift (502 nm → 538 nm) of the lowest energy band occurs with F^-, CN^-, and AcO^- and the visual color change of the complexes is in line with their spectral changes and thus make the complexes suitable colorimetric sensors for selected anions.

Absorption titrations were done to acquire quantitative information regarding receptor-anion interaction process. Spectral changes of **1** and **2** upon incremental addition of selected anions are presented in Figure S35-S38, (SI). In presence of F^-, AcO^-, and CN^- ions, both **1** and **2** exhibit one-step change, although the extent of change varies considerably with the nature of the anions. On gradual addition of the said anions, the band around 500 nm in **1** and **2** gradually decreases in intensity with concomitant evolution of broad band in the range between 520 nm and 660 nm. In both cases, the absorption curves pass through several well defined isosbestic points and spectral saturation occur upon addition of 12 equiv of the anions.

Absorption titration profile of **3** upon gradual addition of selected anions is shown in Figure S39-S42 (SI). In contrast to both **1** and **2**, **3** exhibits two-step changes with each of F^- CN, and AcO^- in almost equal extent, while one-step change in presence of $H_2PO_4^-$. Addition of excess $H_2PO_4^-$ leads to the precipitation of the resulting species. Successive absorption lines are found to pass through several isobestic points in each step. The first step probably corresponds to anion-induced removal of NH protons associated to H_2pbbzim moieties as they are supposed to be more acidic. In the second step, the imidazole NH protons associated with phenyl-benzimidazole groups in tpy-BPhBzimH_2-tpy are deprotonated upon addition of excess anions. Equilibrium constants associated with the deprotonation processes with selected anions were estimated from UV-vis titration data and are summarized in Table 3.

In contrast to most of the terpyridine complexes of Ru(II), the present complexes exhibit moderately strong luminescence at room temperature which in turn was utilized for sensitive detection of selective anions. The band at 660 nm for **1** and at 658 nm for **2** undergoes nominal

in presence of Cl^-, Br^-, I^-, HSO_4^-, and NO_3^- ions. F^-, AcO^-, and CN^- induce significant quenching, while $H_2PO_4^-$ induces remarkable enhancement of luminescence intensity in both cases (Figure S34, SI). In contrast to both **1** and **2**, quenching of luminescence occurs with each of F^-, AcO^-, and CN^- and $H_2PO_4^-$ for **3**, although the extent of change varies with the nature of the anions. Luminescence spectral profiles upon gradual addition of selected anions are shown in Figure S35-S42, (SI). Luminescence titration data were also utilized for estimating the equilibrium constants for the interaction between the complexes and selected anions and the estimated values lie in the six orders of magnitude. Moreover, the estimated values of *K* from both absorption and emission processes were found to correlate reasonably well (Table 3). The limit of detection of the complexes towards selected anions were also calculated from the absorption and emission titration data and were found to lie in the range of 3.20×10^{-9} M - 1.71×10^{-9} M for F^- and between 6.4×10^{-9} M and 2.30×10^{-9} M for CN^- (Figure S43-S54, SI).

As luminescence lifetime-based detection is much more advantageous over intensity-based method (as lifetimes of the species are relatively insensitive to source variation, photo-bleaching of the probe material, and changes in the efficiency of the optical system), we are interested to measure the luminescence lifetimes of the complexes upon incremental addition of selected anion (Figure S55-S57, SI). In absence of the anions, the complexes show grossly mono-exponential decay, but upon gradual addition of the anions the intensity decays show complex kinetics that can be fitted with bi-exponential functions. In line with the steady state behaviors, the lifetimes of both **1** and **2** decrease upon incremental addition of F^- and CN^-. Addition of $H_2PO_4^-$, on the other hand, leads to increase of lifetime in **1**, while small decrease in case of **2**. In contrast to both **1** and **2**, lowering of lifetimes occur in **3** with all the three anions (F^-, CN^-, and $H_2PO_4^-$). Moreover, for a given anion, the extent of lifetime lowering is much greater for **3** compared with both **1** and **2**. Bi-exponential decay profiles in presence of selected anions indicate the presence of at least two distinct luminescent species; anion-bound or depronated form of the receptor whose lifetime is shorter and the free receptor whose lifetime is relatively larger. Thus, significant modulation of luminescence lifetimes can be useful for lifetime based detection of selected anions.

Table S1. Selected Calculated Bond Distances (Å) in the Ground State of **1**, **2**, **3**, **2a**, and **3a** and in the Triplet Excited State of **3** and **3a**.

		Ground state				Excited state	
	1	**2**	**3**	**2a**	**3a**	**3**	**3a**
Ru1-N1	2.1114	2.1108	2.1092	2.1122	2.0978	2.1094	2.0978
Ru1-N2	2.0058	2.0066	2.0006	2.0089	1.9847	2.0004	1.9850
Ru1-N3	2.1110	2.1124	2.1075	2.1130	2.0991	2.1087	2.0990
Ru1-N4	2.1110	2.1121	2.1203	2.1111	2.1176	2.1208	2.1177
Ru1-N5	2.0079	2.0076	2.0432	2.0059	2.0592	2.0424	2.0595
Ru1-N6	2.1114	2.1110	2.1200	2.1109	2.1180	2.1210	2.1180
Ru2-N1'	2.1120	2.1116	2.1103	2.1115	2.0968	2.1181	2.0927
Ru2-N2'	2.0068	2.0067	2.0011	2.0092	1.9839	1.9390	1.9953
Ru2-N3'	2.1111	2.1106	2.1083	2.1107	2.0980	2.1203	2.1273
Ru2-N4'	2.1120	2.1119	2.1213	2.1115	2.1173	2.1146	2.0722
Ru2-N5'	2.0086	2.0081	2.0426	2.0065	2.0601	2.0923	2.0634
Ru2-N6'	2.1123	2.1111	2.1200	2.1114	2.1167	2.1134	2.0728

Table S2. Selected Calculated Bond Angles (deg) in the Ground State of **1**, **2**, **3**, **2a**, and **3a** and in the Triplet Excited State of **3** and **3a**.

		Ground state				Excited state	
	1	**2**	**3**	**2a**	**3a**	**3**	**3a**
N6Ru1N2	101.73	101.87	102.63	101.72	102.84	102.33	102.31
N6Ru1N4	156.77	156.83	154.89	156.92	154.55	154.89	154.47
N6Ru1N5	78.39	78.39	77.43	78.44	77.28	77.44	77.79
N6Ru1N1	92.22	92.12	92.48	92.22	92.36	92.30	89.79
N6Ru1N3	92.35	92.45	92.38	92.39	92.64	92.66	95.02
N2Ru1N1	78.48	78.44	78.49	78.32	78.79	78.53	77.86
N2Ru1N4	101.49	101.29	102.47	101.34	102.59	102.77	102.55
N2Ru1N3	78.42	78.40	78.59	78.32	78.73	78.52	79.88
N4Ru1N5	78.38	78.44	77.46	78.48	77.27	77.44	77.75
N4Ru1N1	92.41	92.34	92.47	92.20	92.46	92.53	89.87
N4Ru1N3	92.24	92.27	92.55	92.37	92.35	92.32	94.87
N5Ru1N1	101.37	101.25	101.92	101.41	101.15	101.47	105.85
N5Ru1N3	101.72	101.89	101.00	101.94	101.32	101.46	96.38
N1Ru1N3	156.90	156.84	157.08	156.64	157.52	157.05	157.75
N2Ru1N5	179.81	179.59	179.58	179.68	179.86	179.77	176.27
N6'Ru2N2'	101.33	101.69	102.37	101.71	102.35	103.71	102.64
N6'Ru2N4'	156.73	156.80	154.89	156.89	154.55	152.47	154.54
N6'Ru2N5'	78.37	78.43	77.43	78.46	77.30	76.2	77.26
N6'Ru2N1'	92.16	92.14	92.48	92.37	92.39	92.23	92.45
N6'Ru2N3'	92.42	92.39	92.46	92.24	92.55	92.62	92.44
N2'Ru2N1'	78.39	78.38	78.47	78.32	78.83	79.40	78.74
N2'Ru2N4'	101.93	101.50	102.74	101.39	103.09	103.80	102.81
N2'Ru2N3'	78.43	78.46	78.55	78.35	78.75	79.40	78.77
N4'Ru2N5'	78.36	78.37	77.45	78.43	77.25	76.27	77.27
N4'Ru2N1'	92.52	92.33	92.51	92.27	92.38	92.51	92.55
N4'Ru2N3'	92.16	92.37	92.46	92.39	92.48	92.65	92.38
N5'Ru2N1'	101.81	101.70	101.68	101.51	100.98	101.11	101.23
N5'Ru2N3'	101.35	101.44	101.28	101.81	101.43	100.00	101.24
N1'Ru2N3'	156.82	156.85	157.03	156.67	157.58	158.80	157.51
N2'Ru2N5'	179.84	179.84	179.74	179.76	179.60	179.46	179.91

Table S3. Selected Molecular Orbital along with their Energies and Compositions of **1**, **2**, and **3** in the Ground State.

Ground State															
	1					**2**					**3**				
MO	Energy /eV	bi-phen	lig tpy	mpt cap	Ru	Energy /eV	bi-phen	lig tpy	pyrene tpy	Ru	Energy /eV	bi-phen	lig tpy	bzimd	Ru
LUMO+3	-2.69	0.0	1.8	90.3	7.8	-2.72	0.0	1.5	90.6	7.7	-2.63	0.0	1.3	90.8	7.7
LUMO+2	-2.69	0.0	1.7	90.4	7.8	-2.72	0.0	1.8	90.4	7.7	-2.63	0.0	1.3	90.9	7.7
LUMO+1	-2.76	2.9	87.2	1.8	7.9	-2.76	2.9	87.2	1.8	7.8	-2.73	2.9	87.6	1.3	7.9
LUMO	-2.77	3.5	86.8	1.7	7.8	-2.77	3.5	87.0	1.6	78	-2.74	3.5	87.1	1.3	7.9
HOMO	-5.67	79.4	16.32	0.0	3.8	-5.66	0.8	0.7	93.2	5.1	-5.67	79.1	16.3	0.4	4.1
HOMO-1	-6.04	34.0	28.8	3.7	33.4	-5.67	0.5	0.7	93.7	4.9	-5.90	0.0	11.1	29.3	59.4
HOMO-2	-6.12	0.0	6.7	33.0	60.2	-5.67	78.3	15.8	2.1	3.6	-5.90	0.0	11.0	29.4	59.4
HOMO-3	-6.12	0.0	6.6	33.2	60.0	-6.05	35.4	28.8	3.5	32.0	-6.03	32.0	28.9	3.5	35.4

Table S4. Selected Molecular Orbital along with their Energies and Compositions in the Ground State of **2a** and **3a** and in the Triplet Excited State of **3** and **3a**.

Ground State										
	2a					**3a**				
MO	Energy /eV	bi-phen	lig tpy	pyrene tpy	Ru	Energy /eV	bi-phen	lig tpy	bzimd	Ru
LUMO+3	-2.58	2.1	88.8	1.6	7.4	-2.0	0.0	97.8	0.0	2.0
LUMO+2	-2.59	1.8	89.0	1.6	7.5	-2.0	0.0	97.8	0.0	1.9
LUMO+1	-2.65	0.0	1.6	90.4	7.9	-2.13	1.8	85.1	1.9	11.0
LUMO	-2.65	0.0	1.7	90.3	7.9	-2.14	1.8	85.0	1.9	11.1
HOMO	-4.46	82.3	11.2	5.7	0.6	-4.33	86.6	11.5	0.0	1.5
HOMO-1	-4.99	81.0	12.8	5.1	1.0	-4.78	0.0	8.5	43.9	47.4
HOMO-2	-5.05	89.5	7.2	2.6	0.6	-4.78	0.0	8.5	44.0	47.4
HOMO-3	-5.39	80.7	13.6	3.4	2.1	-4.83	16.3	16.3	0.0	6.4
Triplet Excited State										
	3					**3a**				
MO	Energy /eV	bi-phen	lig tpy	bzimd	Ru	Energy /eV	bi-phen	lig tpy	bzimd	Ru
LUMO+3	-2.63	0.0	1.4	90.8	7.7	-2.0	0.0	97.8	0.0	1.9
LUMO+2	-2.65	0.0	1.2	92.2	6.4	-2.03	0.0	95.5	0.0	3.4
LUMO+1	-2.74	3.4	87.3	1.3	7.9	-2.13	1.8	85.1	1.9	11.0
LUMO	-2.91	6.1	81.4	1.7	10.6	-2.28	1.2	84.6	2.8	11.2
HOMO	-5.58	65.0	22.6	1.2	11.0	-4.32	85.9	11.7	0.0	1.9
HOMO-1	-5.90	0.0	11.1	29.4	59.4	-4.65	3.4	11.8	40.9	43.8
HOMO-2	-5.94	2.4	12.5	27.9	57.0	-4.78	0.0	8.5	44.0	47.4
HOMO-3	-5.96	25.2	30.0	6.1	38.6	-4.83	75.2	15.4	2.2	6.9

Table S5. Selected UV-vis Absorption Energy Transitions at the TD-DFT/B3LYP Level for **1**, **2,** and **3** in Dimethylsulfoxide.

Excited state	λ_{cal}/nm/ε_{cal}/ M^{-1} cm^{-1}	Oscillator strength(f)	λ_{expt}/nm/ ε_{expt}/ M^{-1} cm^{-1}	Key transitions	Character
1					
S_6	484(172275)	0.88	499(58,500)	H→L (31%), H-6→L +3(20%), H→L+3 (13%), H-2→L (5%), H-2→L+1 (5%)	ILCT, MLCT
S_{25}	422(71032)	0.32	452(27910)	H-5→L+4 (89%), H-1→L (3%), H-1→L+1 (3%)	MLCT, ILCT
S_{31}	366(150573)	1.27	360(37,770)	H→L+8 (59%), H-8→L (16%), H-8→L+1 (13%)	ILCT,π-π*
S_{139}	302 (214818)	0.36	316(1,25,500)	H-16→L+3 (15%), H-4→L+14 (20%), H-4→L+15 (12%), H-16→L (6%), H-16→L +1(6%), H-5→L +15 (7%), H-9→L +6 (5%),	π-π*
2					
S_3	499(197978)	1.61	500(55,500)	H→L+2 (54%), H-2→L (13%), H-1→L +3(14%), H-7→L+2 (4%)	ILCT, MLCT
S_{33}	421(72521)	0.36	450 (25980)	H-5→L+4 (82%), H-8→L+3(7%)	MLCT, ILCT
S_{60}	366(236820)	1.47	377(48,250)	H-10→L(16%), H-10→L+1 (14%), H-2→L+10 (54%)	ILCT, π-π*
S_{131}	302(204288)	0.50	315(116250)	H-19→L +3(45%), H-5→L+14 (37%)	π-π*
3					
S_7	481(173477)	1.02	502(49,400)	H→L (54%), H-5→L +3(3%), H-4→L (7%), H-4→L+1 (4%), H-3→L+1 (9%), H-2→L+7 (7%), H→L+1 (9%)	ILCT, MLCT
S_{16}	440(60885)	0.18	466(29830)	H-6→L+2 (13%), H-3→L (17%), H-3→L+1 (15%), H-1→L+4 (17%), H→L (9%), H→L+1 (9%)	MLCT, ILCT
S_{51}	365(214367)	1.23	380(50,750)	H→L+8 (61%), H-8→L (15%), H-8→L+1 (12%)	ILCT, π-π*
S_{70}	345 (178902)	0.83	351 (1,14,920)	H-11→L+2 (64%), H-10→L+3 (32%)	π-π*
S_{131}	307(270991)	0.30	319 (1,22,250)	H-19→L (35%), H-19→L+1 (33%), H-9→L+4 (11%), H-1→L +13(5%),	π-π*

Table S6. Selected UV-vis Absorption Energy Transitions at the TD-DFT/B3LYP Level for **2a** and **3a** in Dimethylsulfoxide.

Excited state	λ_{cal}/nm/ε_{cal}/ M^{-1} cm^{-1}	Oscillator strength(f)	λ_{expt}/nm/ ε_{expt}/ M^{-1} cm^{-1}	Key transitions	Character
2a					
S_1	764(23490)	0.49	734 (5530)	H→L +2(66%), H→L (22%), H→L+1 (11%)	ILCT
S_9	584(47309)	0.51	545(30540)	H-2→L +2(23%), H-1→L (11%), H-1→L+3 (54%)	ILCT
S_{29}	494(118382)	0.59	506(41900)	H-4→L +1(54%), H-3→L+2 (19%), H-3→L+3 (12%)	ILCT/MLCT
S_{65}	420(97951)	0.72	375(45720)	H-8→L +4(14%), H→L+18 (34%), H-7→L+5 (14%)	π-π*
S_{115}	362(113957)	0.72	318(85220)	H-4→L +9(62%), H-5→L+8 (22%)	π-π*
3a					
S_3	641(23452)	0.64	662(4180)	H→L (96%),	ILCT
S_{11}	519(68538)	0.66	537(40660)	H-4→L (27%), H-3→L (58%)	ILCT/MLCT
S_{35}	439(110428)	1.02	401(5470)	H→L+8 (83%)	ILCT
S_{79}	379 (111805)	0.48	361(109050)	H-4→L+8 (29%), H-3→L+9 (48%), H-8→L+8 (7%)	π-π*
S_{114}	355(144403)	0.43	325(110430)	H-11→L +4(42%), H-7→L+11 (39%), H-7→L+6 (8%)	π-π*

Table S7. Experimental Luminescence Data of **1**, **2, 3** and **3a** in Dimethylsulfoxide Along with the Calculated Triplet Emission of **3** and **3a**.

Compds	Experiment	Theory
1	660nm	
2	658 nm	
3	687 nm	790 nm
3a	760 nm	988 nm

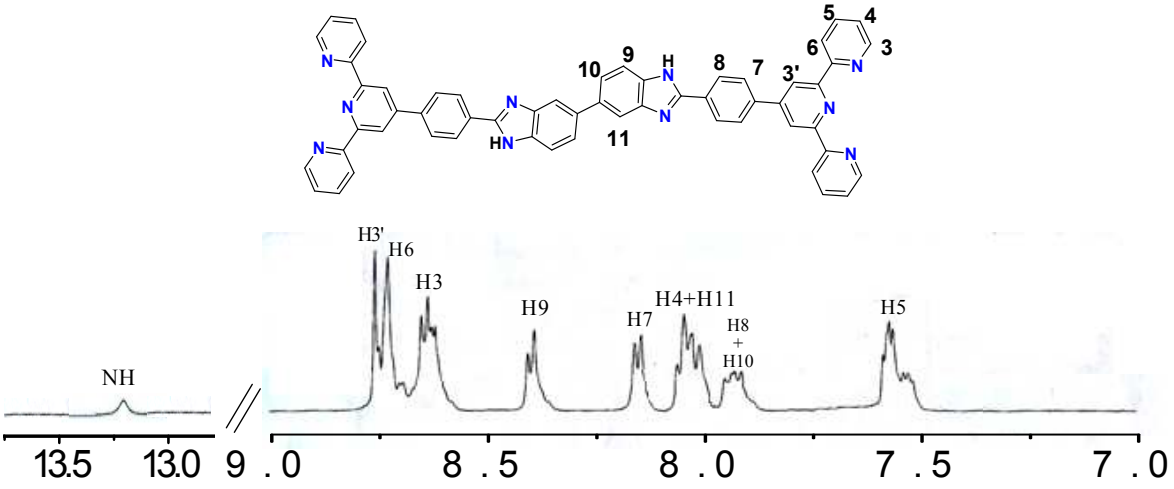

Figure S1. ^{1}H NMR (500 MHz) spectrum of **tpy-BPhBzimH$_2$-tpy** in DMSO-d_6 at room temperature.

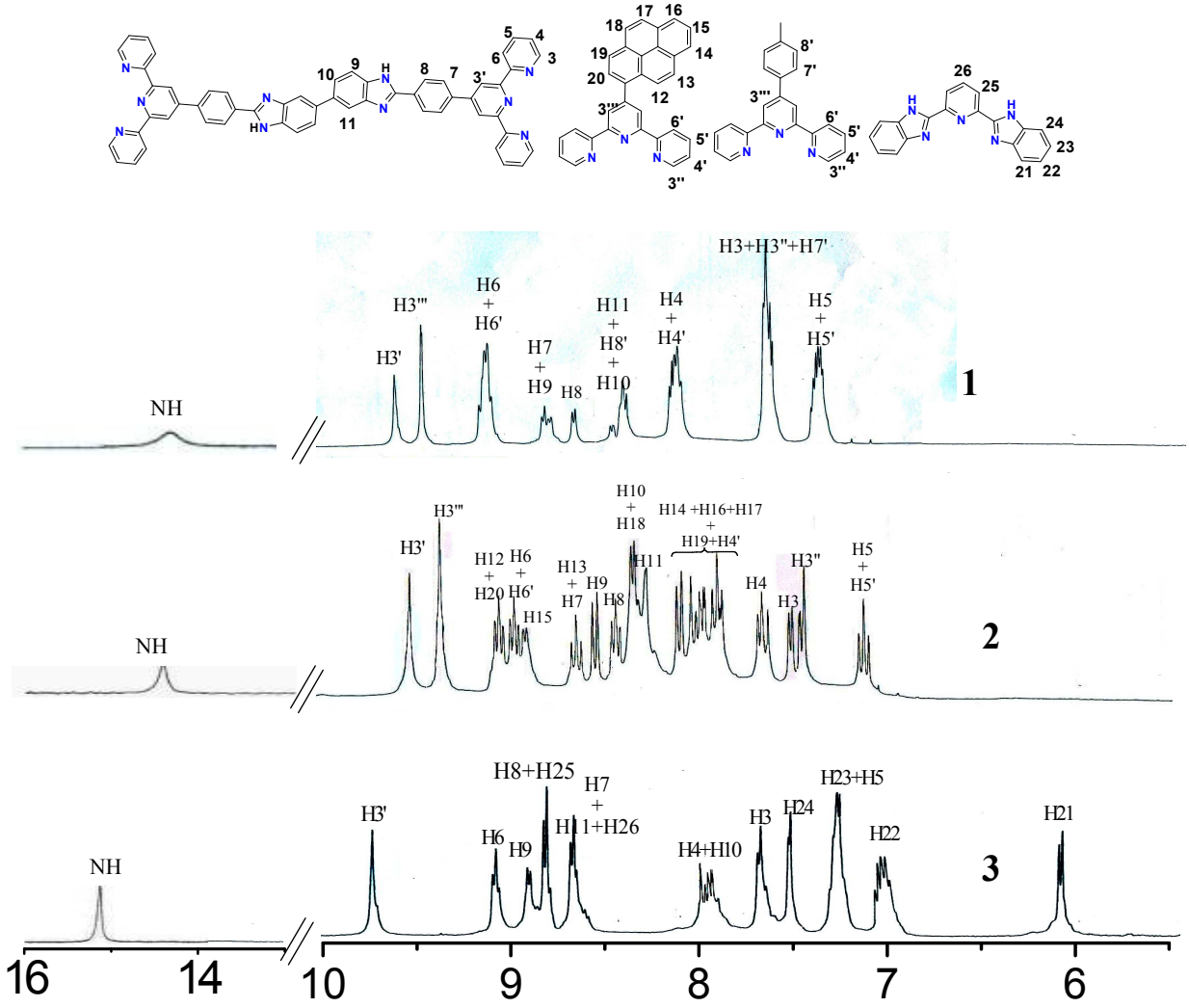

Figure S2. ^{1}H NMR (500 MHz) spectra of **1-3** in DMSO-d_6. The proton numbering is shown on the top.

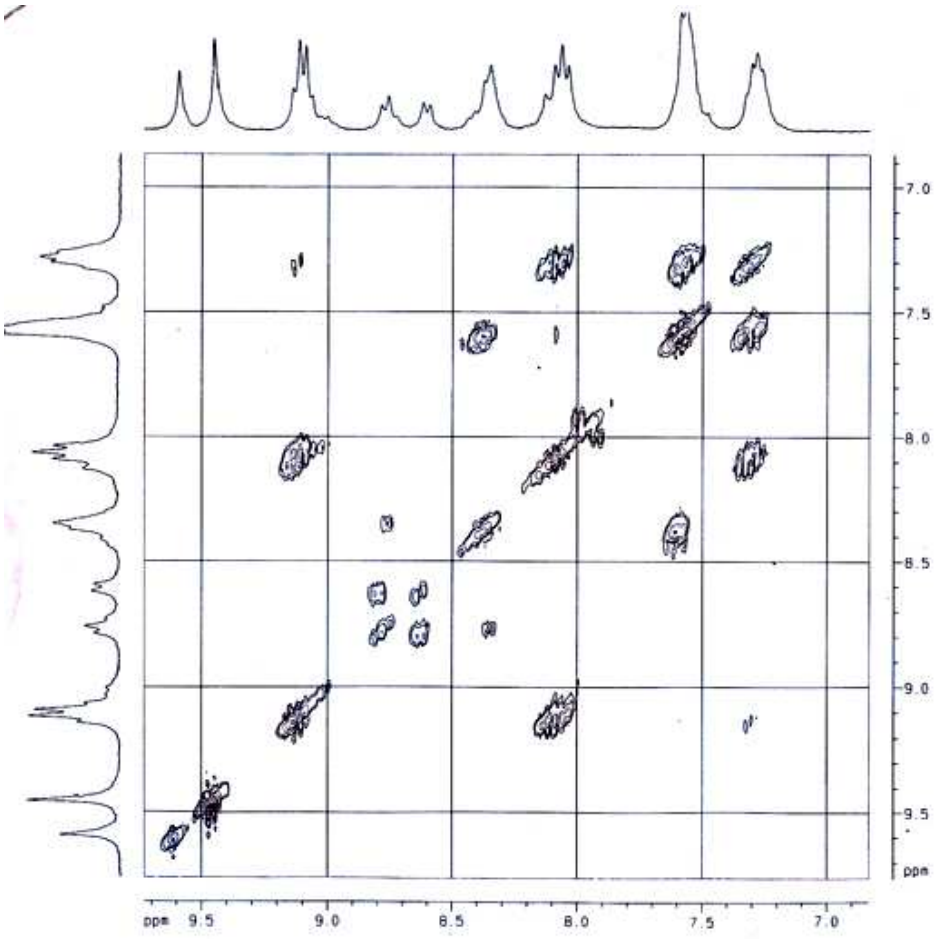

Figure S3. {^{1}H-^{1}H} COSY NMR spectrum of **1** in DMSO-d_6.

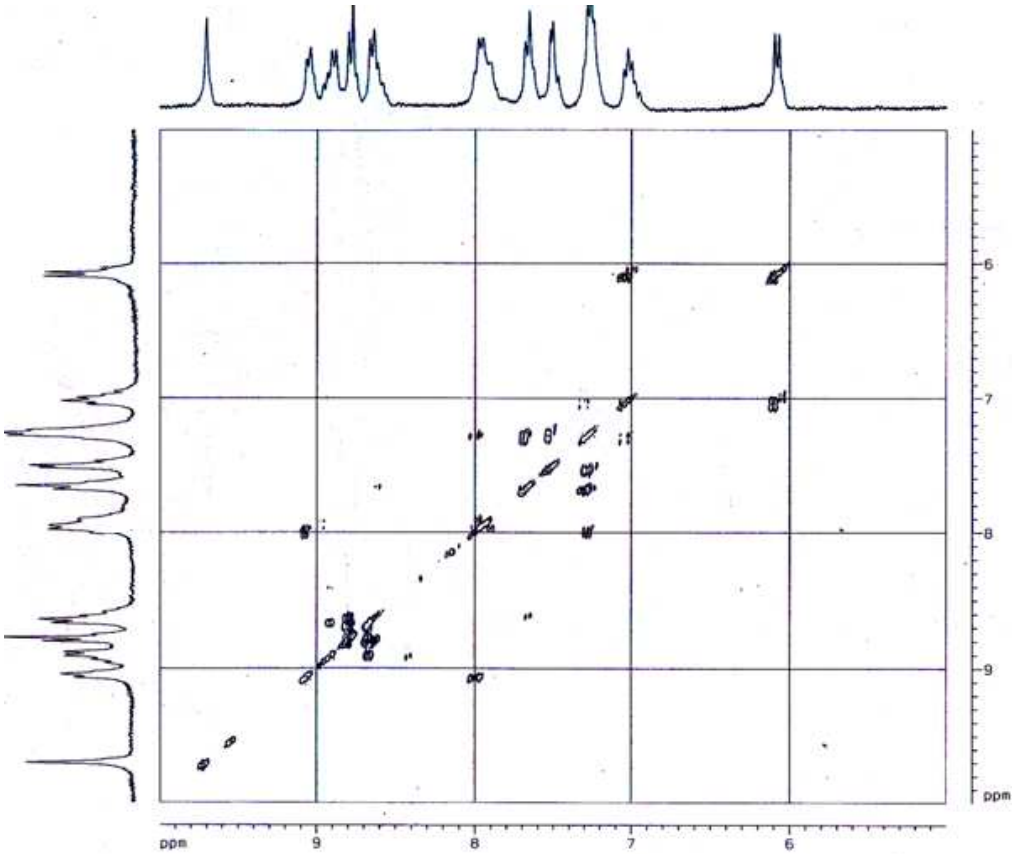

Figure S4. {^{1}H-^{1}H} COSY NMR spectrum of **3** in DMSO-d_6.

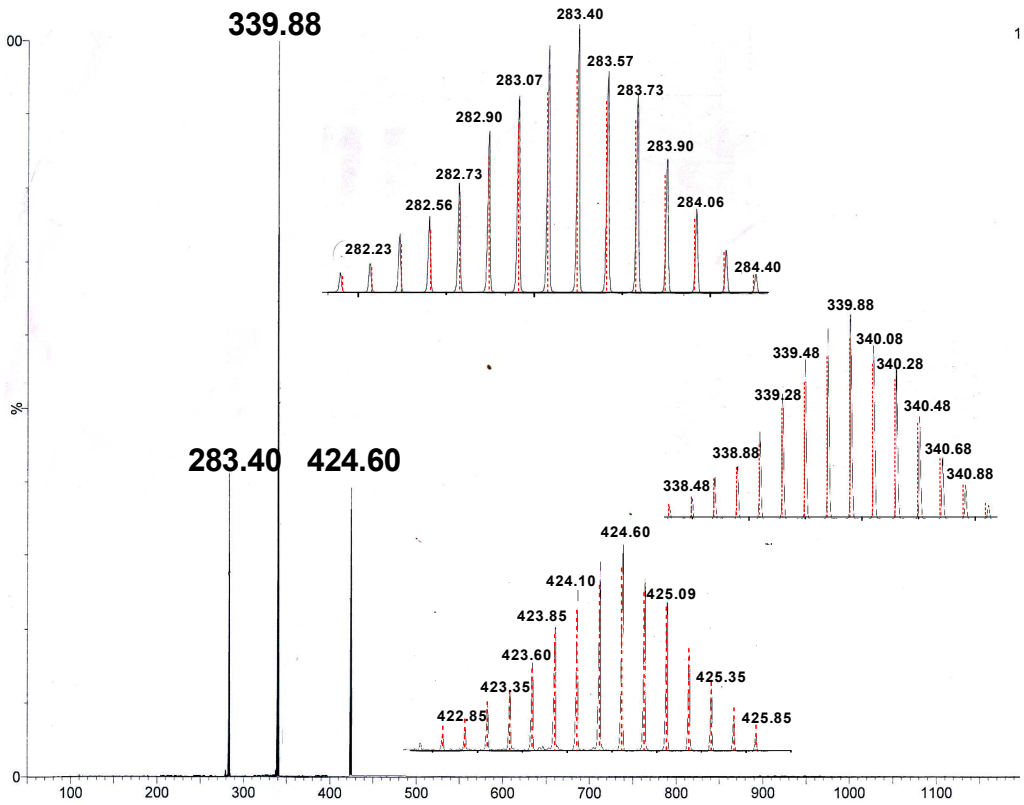

Figure S5. ESI-MS (positive) spectrum for the complex cations of **1**, [(tpy-C_6H_4-CH_3) Ru(tpy-BPhBzimH_4-tpy)Ru(tpy-C_6H_4-CH_3)]$^{6+}$ (m/z=283.40) [(tpy-C_6H_4-CH_3)Ru(tpy-BPhBzimH_3-tpy) Ru(tpy-C6H4-CH_3)]$^{5+}$ (m/z=339.88) and [(tpy-C_6H_4-CH_3)Ru(tpy-PhBzimH_4-tpy) Ru(tpy-C_6H_4-CH_3)]$^{4+}$ (*m/z* = 424.60) in acetonitrile showing observed and simulated isotopic distribution patterns.

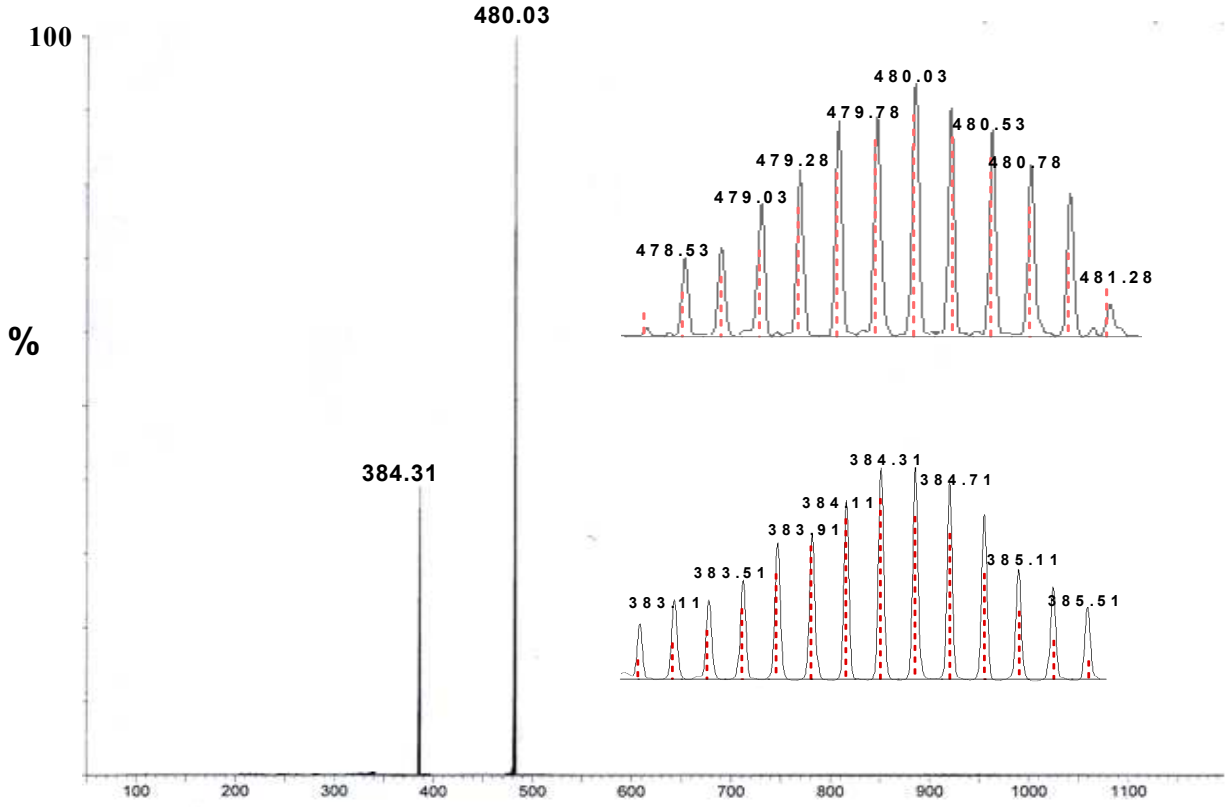

Figure S6. ESI-MS (positive) spectrum for the complex cations of **2**, [(tpy-py)Ru(tpy-BPhBzimH$_3$-tpy)Ru(tpy-py)]$^{5+}$ (*m/z* = 384.31), [(tpy-py)Ru(tpy-BPhBzimH$_2$-tpy)Ru(tpy-py)]$^{4+}$ (*m/z*=480.03) in acetonitrile showing observed and simulated isotopic distribution patterns.

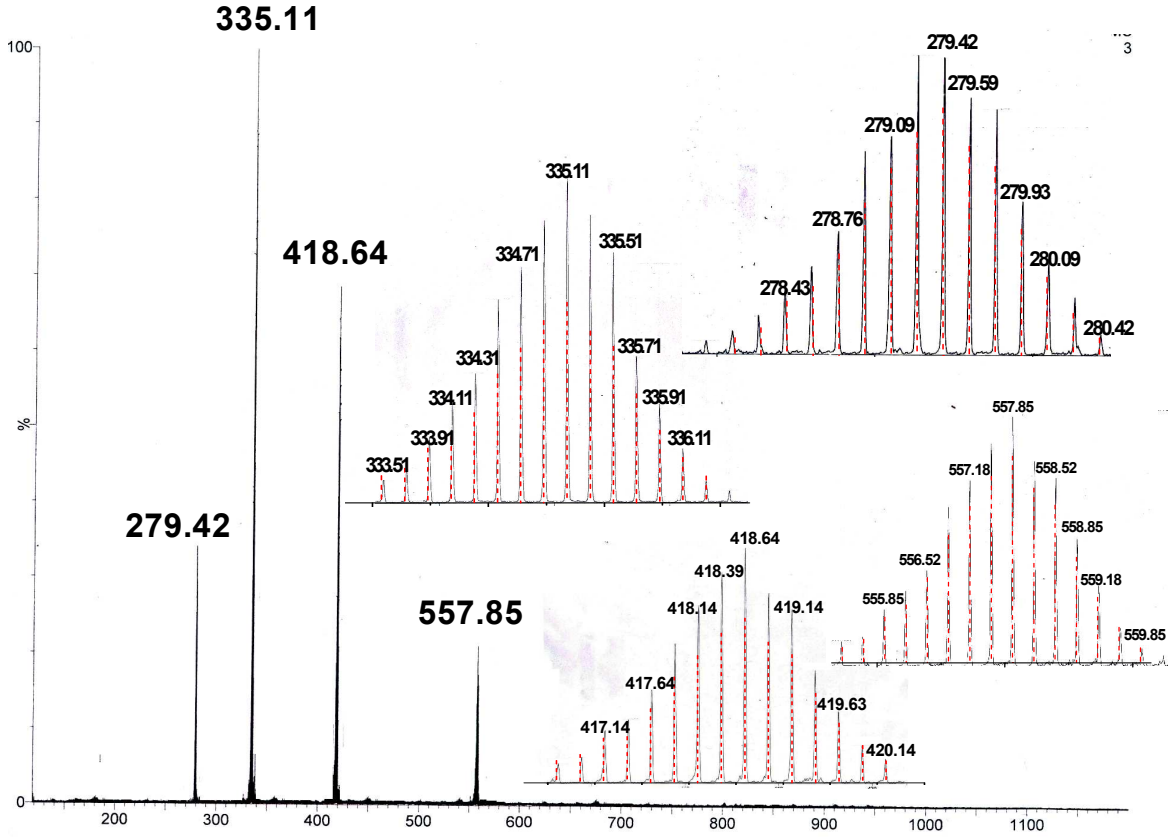

Figure S7. ESI-MS (positive) spectrum for the complex cations of **3**, $[(H_2pbbzim)Ru(tpy\text{-}BPhBzimH_4\text{-}tpy)Ru(H_2pbbzim)]^{6+}$ (*m/z* = 279.42), $[(H_2pbbzim)Ru(tpy\text{-}BPhBzimH_3\text{-}tpy)Ru(H_2pbbzim)]^{5+}$ (*m/z* = 335.11), $[(H_2pbbzim)Ru(tpy\text{-}BPhBzimH\text{-}tpy)Ru(H_2pbbzim)]^{4+}$ (*m/z* = 418.64) and $[(Hpbbzim)Ru(tpy\text{-}BPhBzimH_2\text{-}tpy)Ru(H_2pbbzim)]^{3+}$ (*m/z* = 557.85) in acetonitrile showing observed and simulated isotopic distribution patterns.

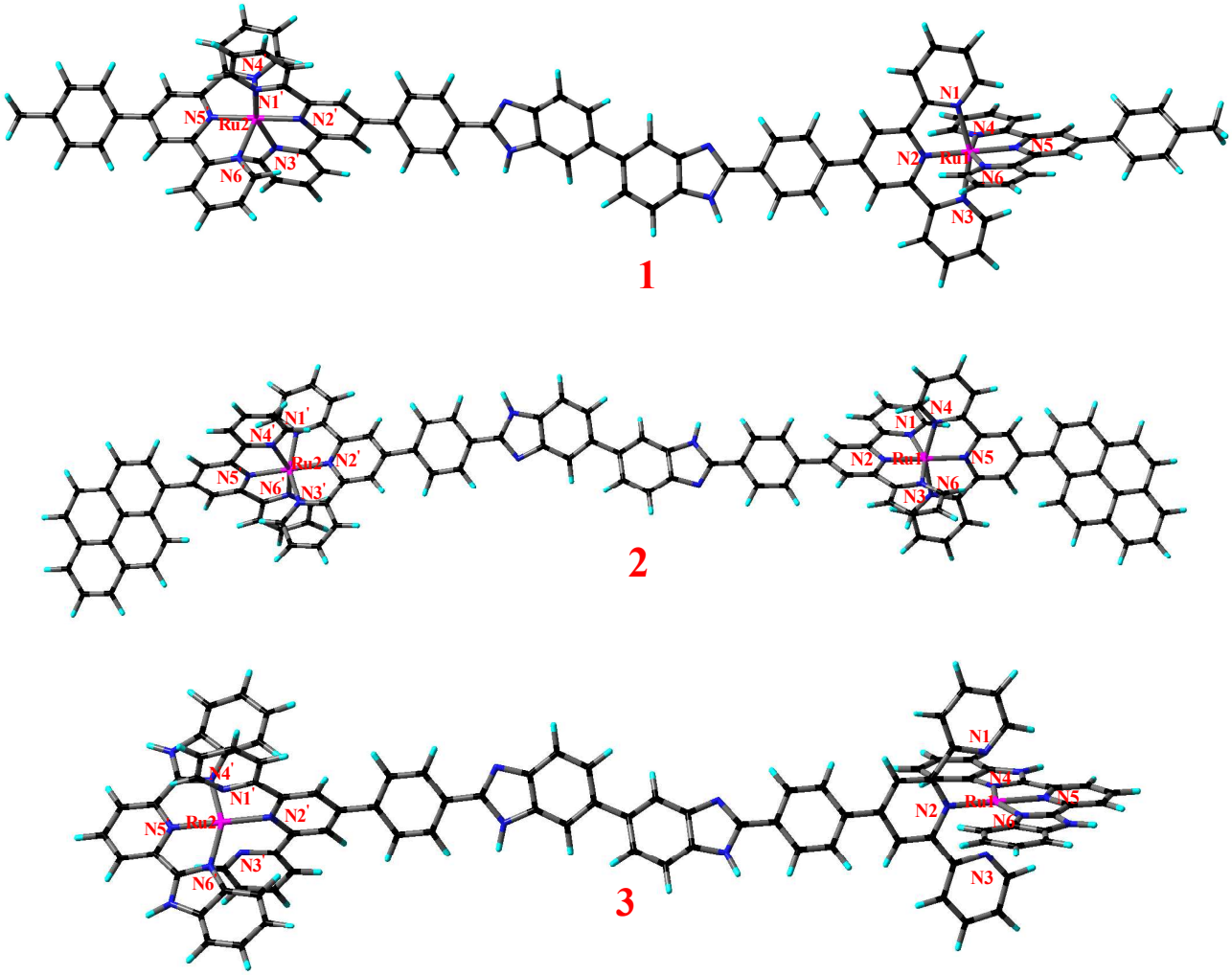

Figure S8. Optimized geometries and labeling schemes of **1**, **2**, and **3** in dimethylsulfoxide.

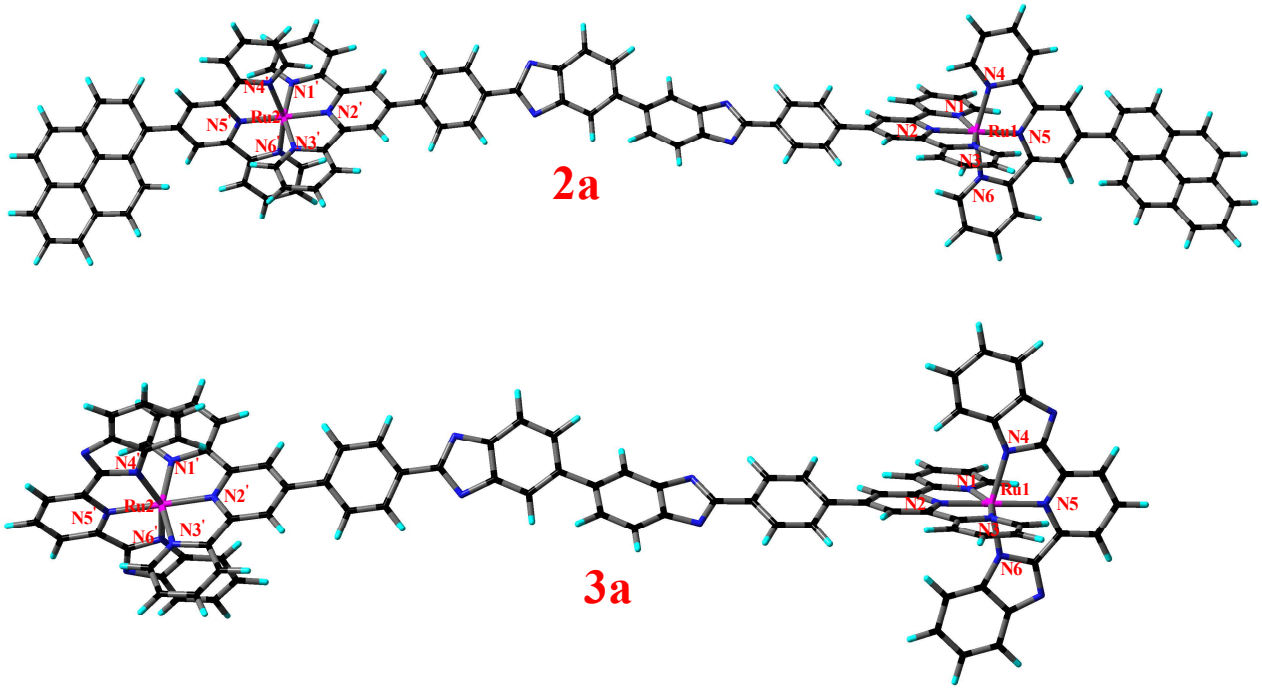

Figure S9. Optimized geometries and labeling schemes of **2a** and **3a** in dimethylsulfoxide.

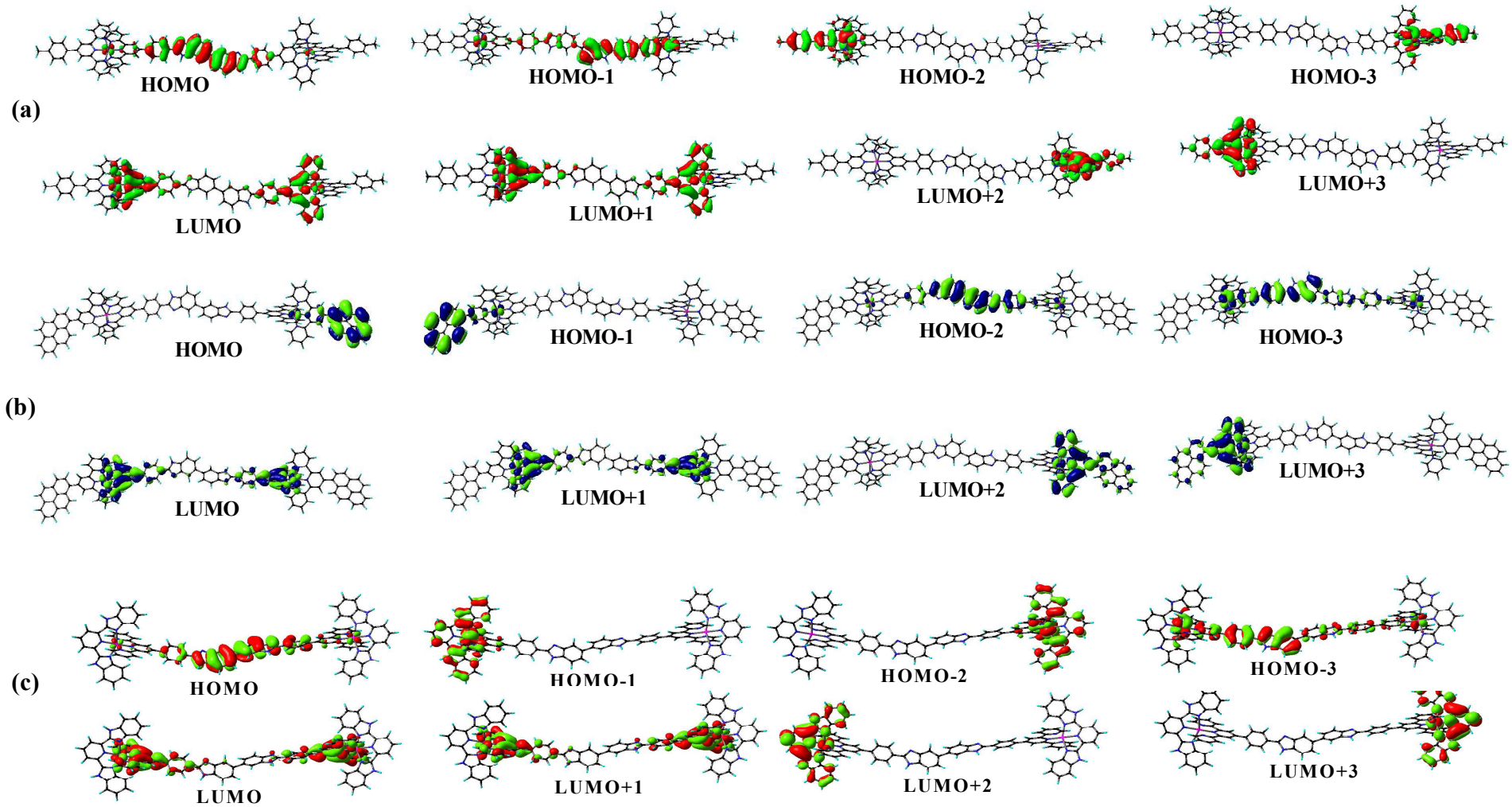

Figure S10. Schematic drawings of the selective frontier molecular orbital of **1**(a), **2** (b), and **3** (c) in the ground state.

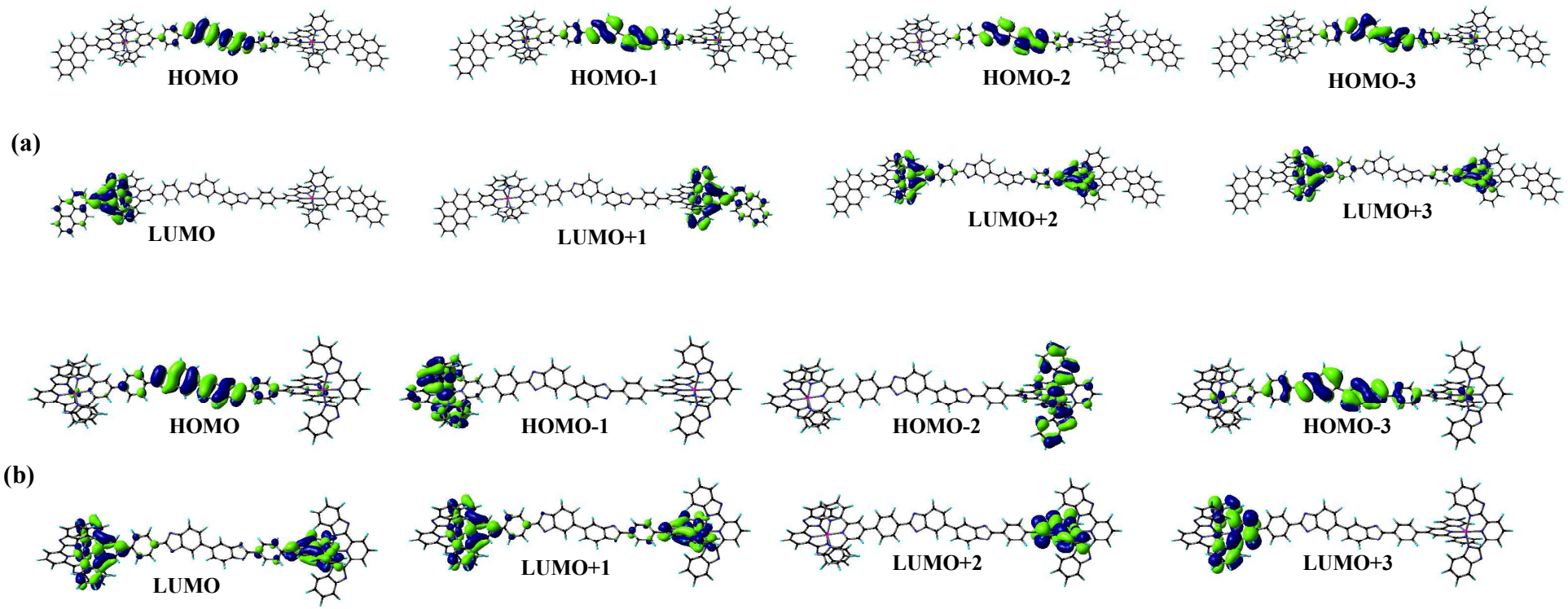

Figure S11. Schematic drawings of the selective frontier molecular orbital of **2a** (a), and **3a** (b) in the ground state.

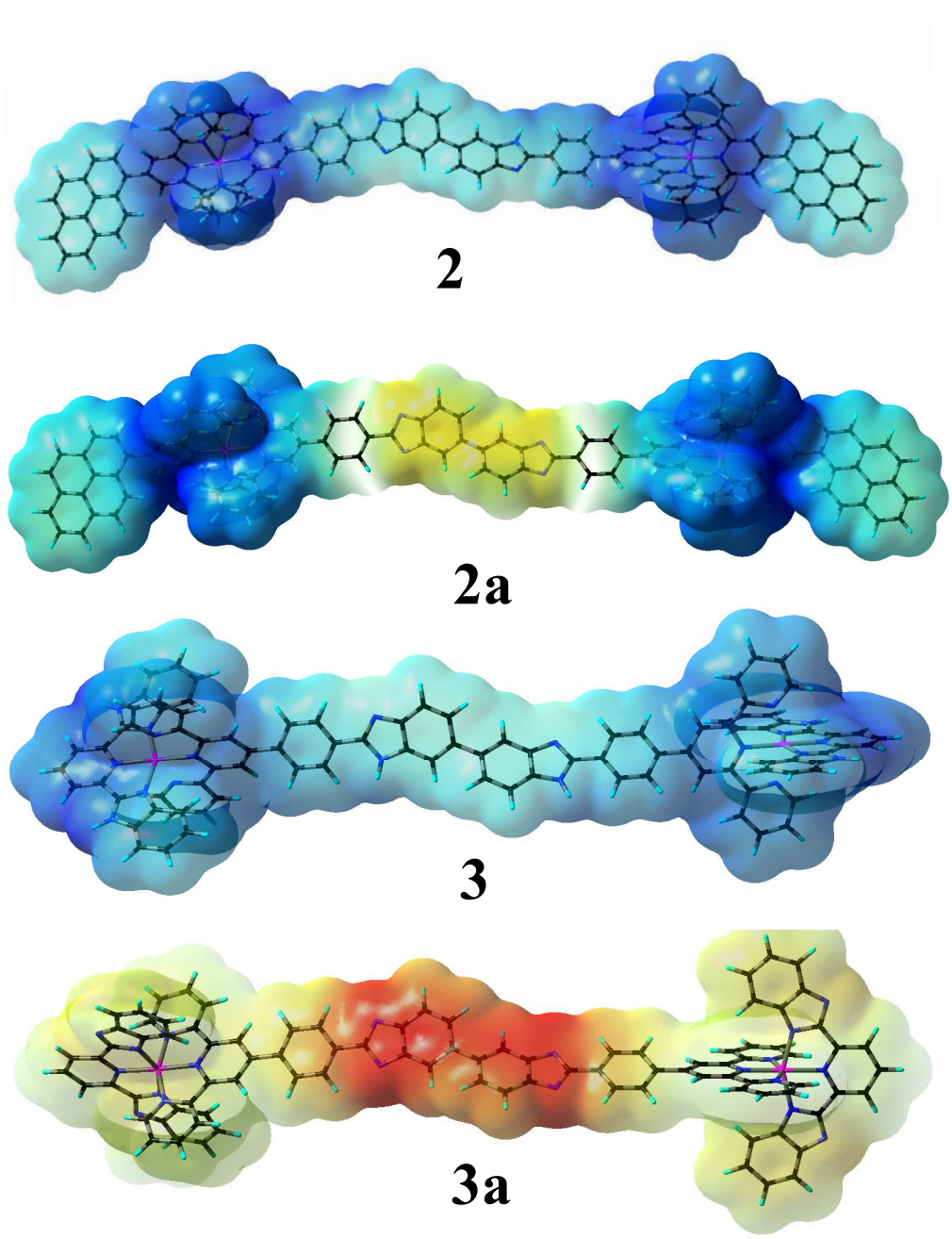

Figure S12. Molecular electrostatic potential (ESP) mapped on the isodensity surface in the ground state for **2**, **2a**, **3**, and **3a** in the range from −0.287 (red) to +0.287 (blue).

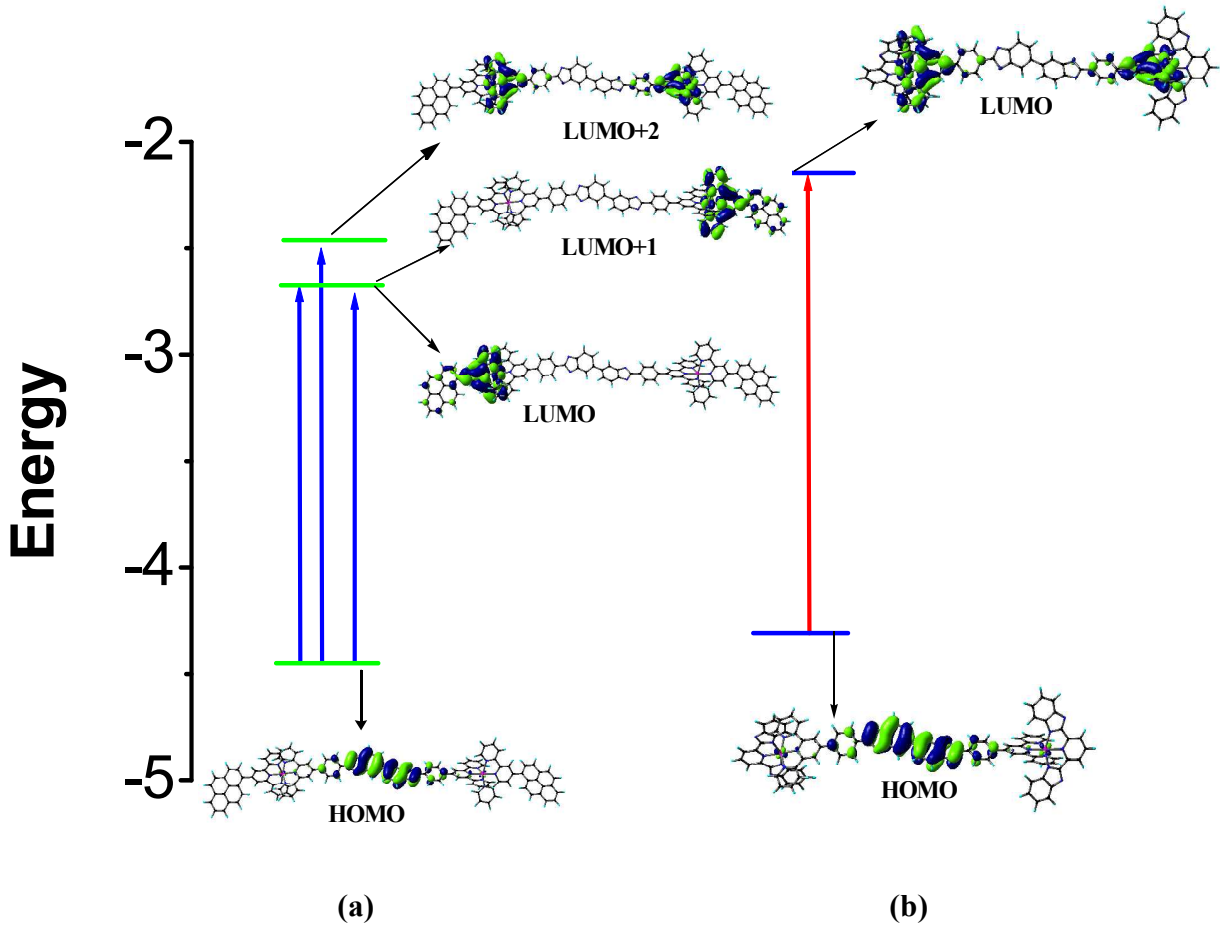

Figure S13. Energy level diagrams depicting the dominant transitions arising out from S_9 state for **2a** (a) and S_3 state for **3a** (b) in dimethylsulfoxide.

		Hole	Electron
1	**484 nm** **S_6**	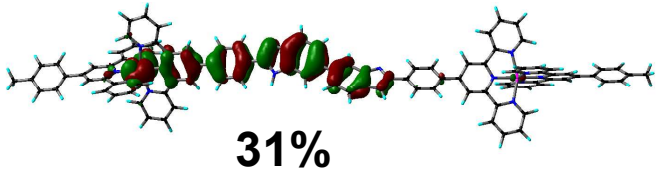 **31%**	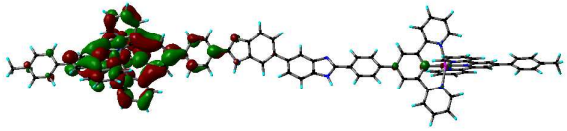
		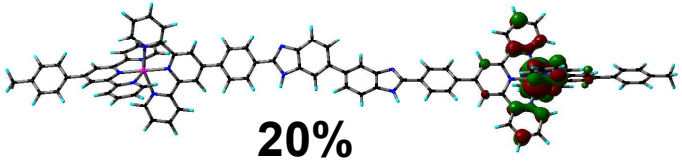 **20%**	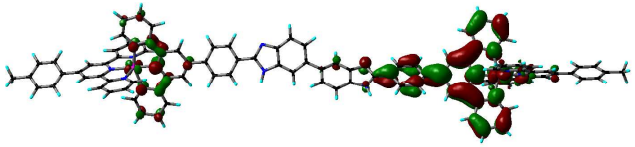
		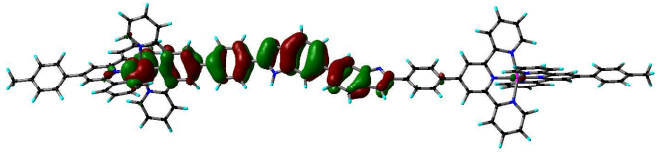 **13%**	

Figure S14. NTOs illustrating the nature of optically active singlet excited states in the absorption bands at 484 nm for **1**. The occupied (holes) and unoccupied (electrons) NTO pairs that contribute more than 10% to each excited state are only represented. All transitions are mixed ^{1}MLCT/^{1}ILCT in character.

		Hole	Electron
2	**499 nm** **S_3**	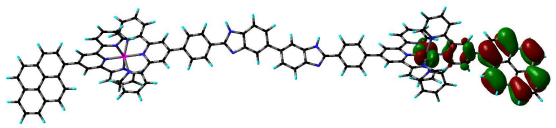	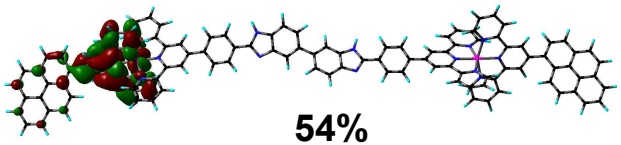 **54%**
		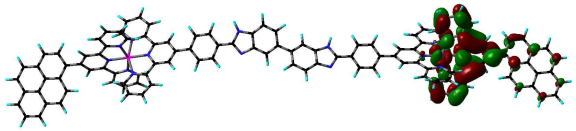	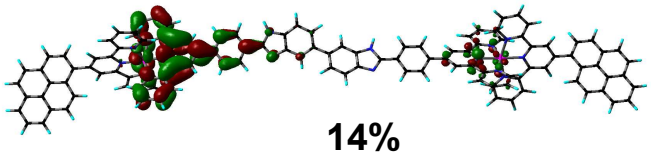 **14%**
		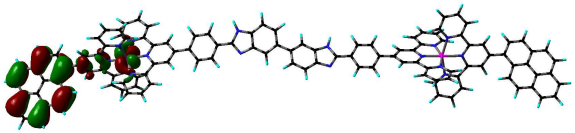	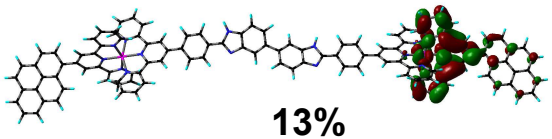 **13%**

Figure S15. NTOs illustrating the nature of optically active singlet excited states in the absorption bands at 499 nm for **2**. The occupied (holes) and unoccupied (electrons) NTO pairs that contribute more than 10% to each excited state are only represented. All transitions are mixed ^{1}MLCT/^{1}ILCT in character.

		Hole	Electron
3	**481nm** S_7	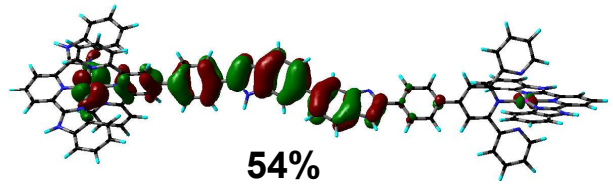 **54%**	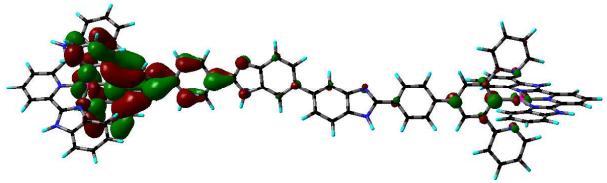
		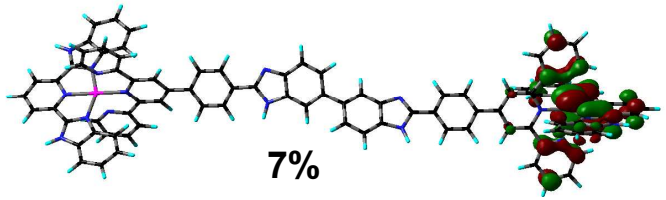 **7%**	
		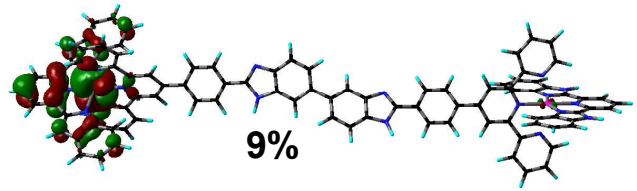 **9%**	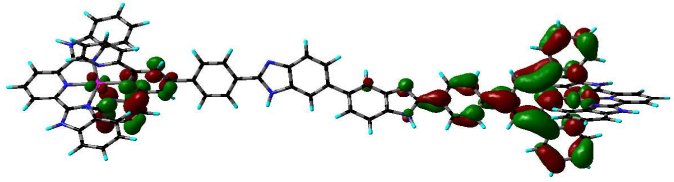

Figure S16. NTOs illustrating the nature of optically active singlet excited states in the absorption bands at 481 nm for **3**. The occupied (holes) and unoccupied (electrons) NTO pairs that contribute more than 5% to each excited state are only represented. All transitions are mixed ^{1}MLCT/^{1}ILCT in character.

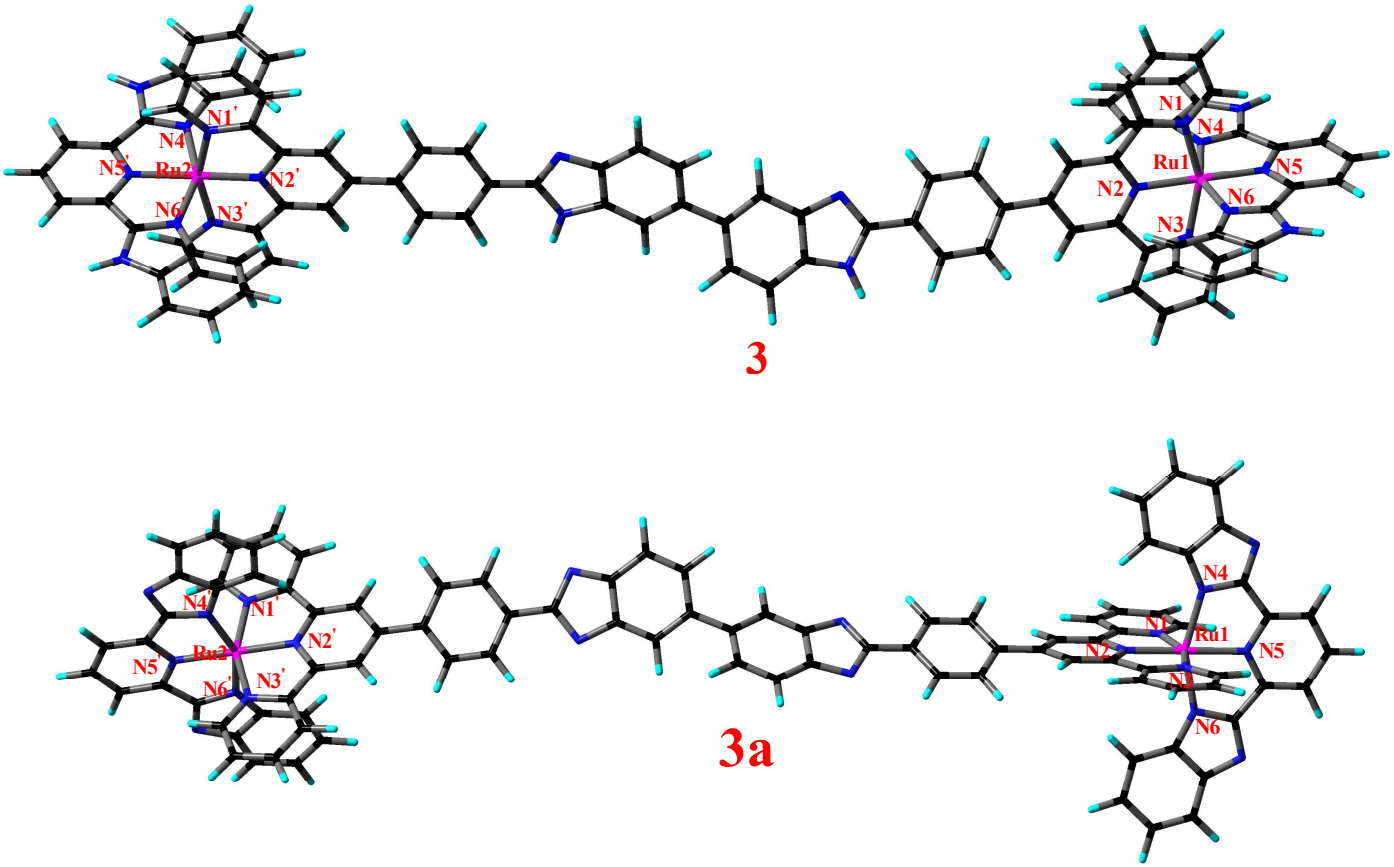

Figure S17. Optimized geometries for **3** and **3a** in the triplet excited state.

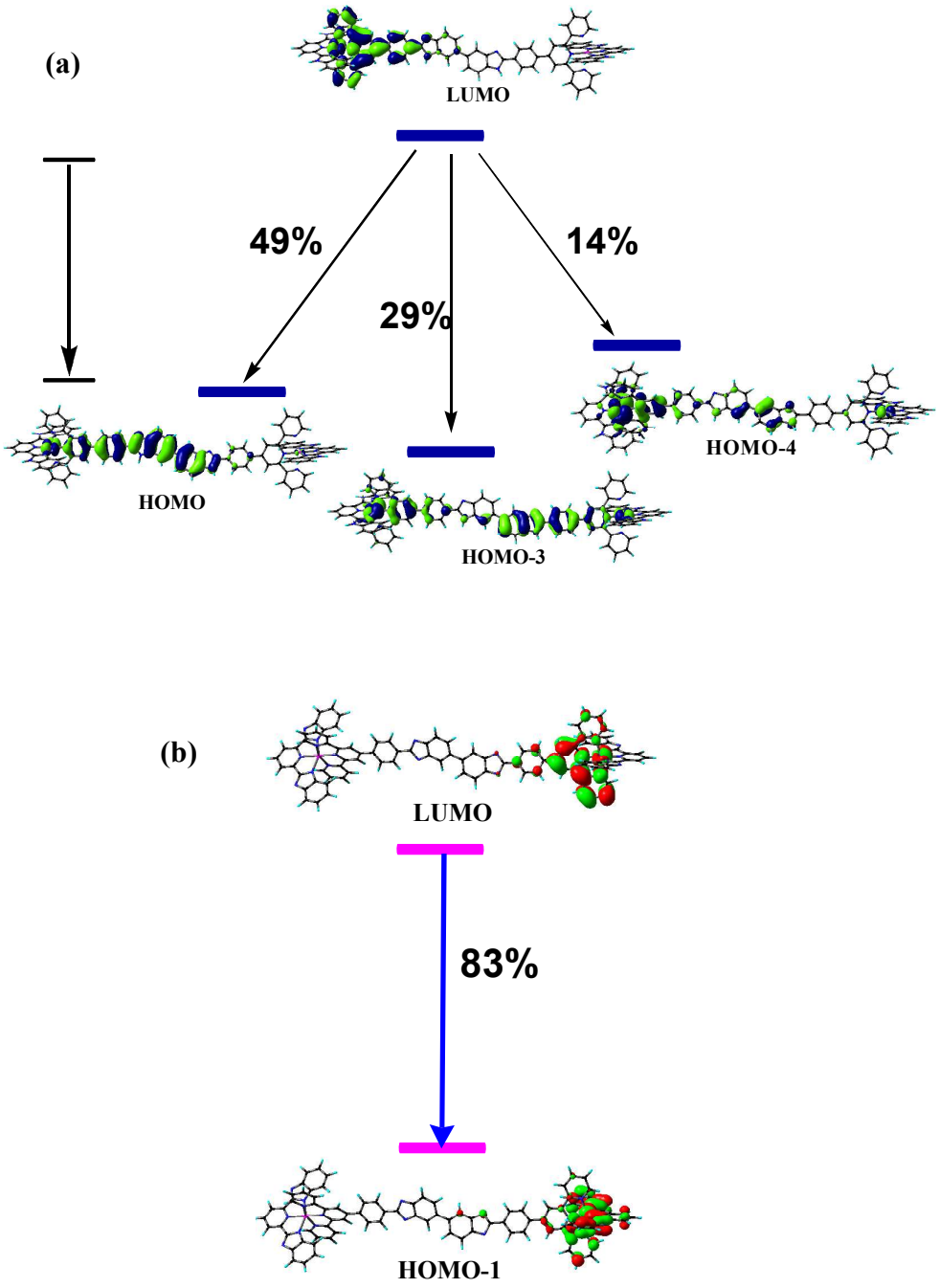

Figure S18. Calculated single electron transitions for the emissions of T_1 states for **3** (a) and **3a** (b).

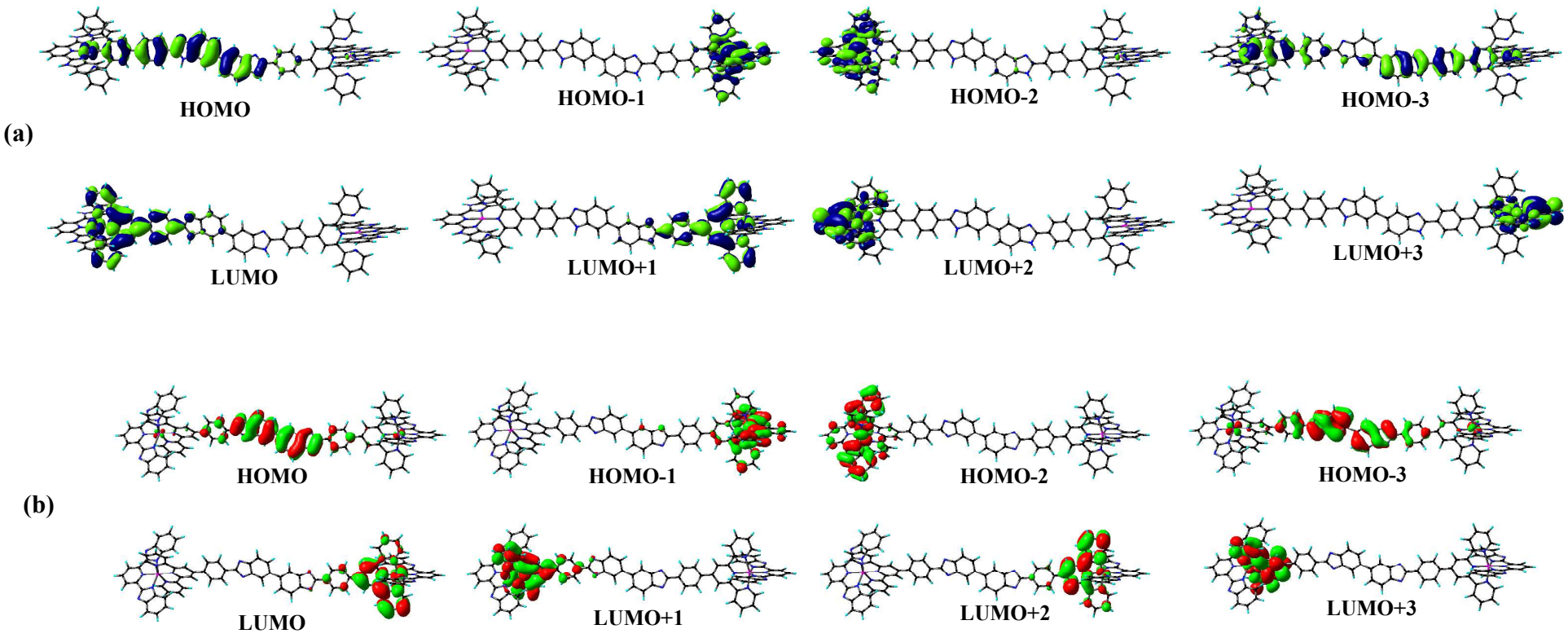

Figure S19. Schematic drawings of the selective frontier molecular orbital of **3** (a) and **3a** (b) in the triplet excited state.

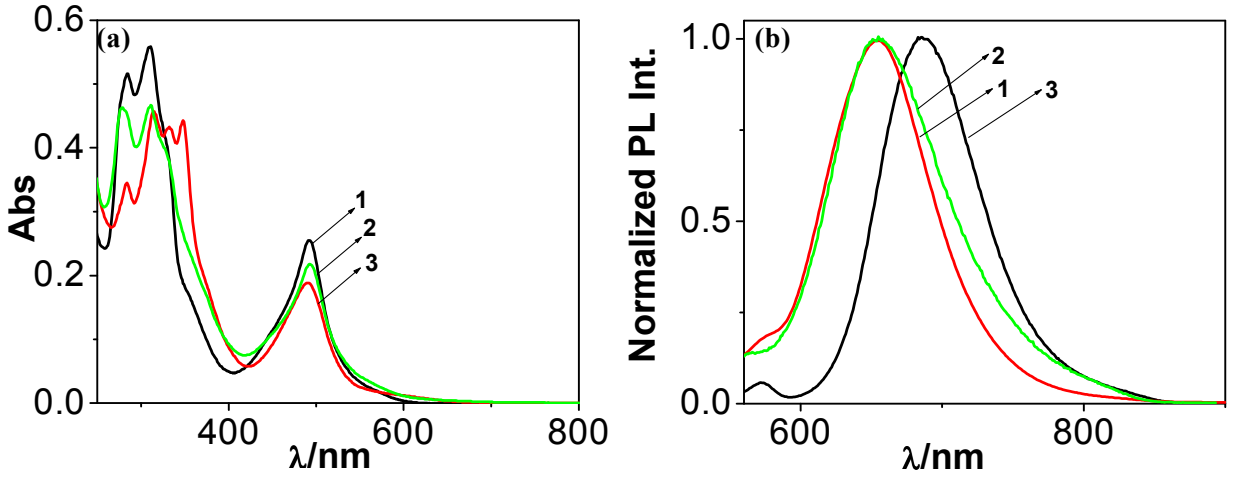

Figure S20. UV-vis absorption (a) and normalized luminescence (b) spectra for **1-3** in acetonitrile at room temperature. Excitation wavelength for recording luminescence spectra is 490 nm.

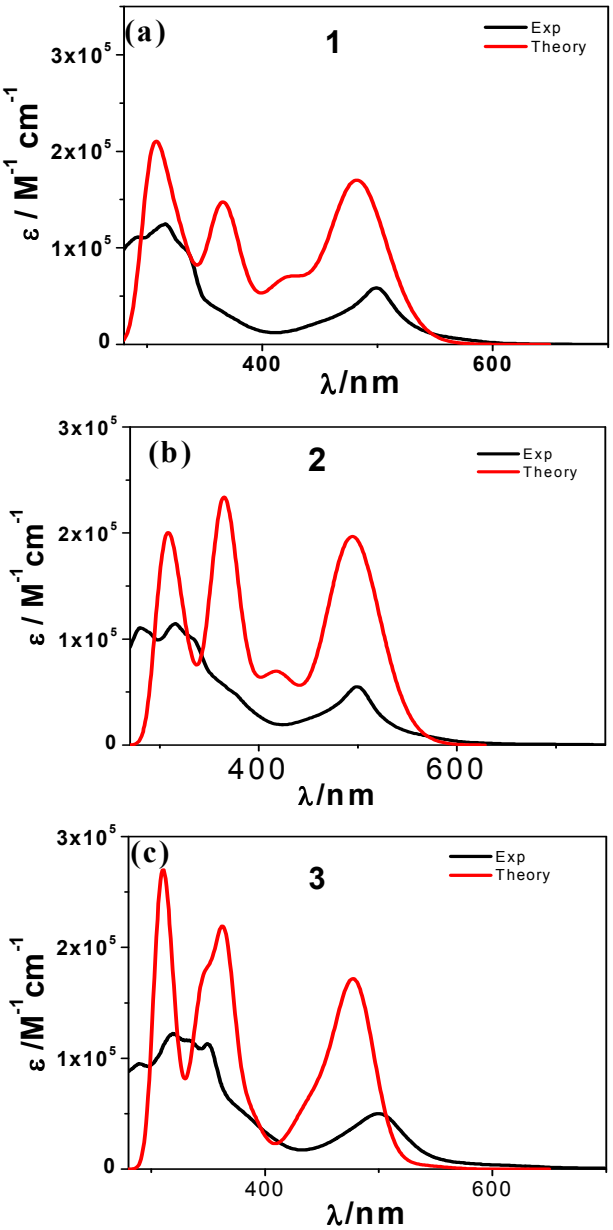

Figure S21. Experimental and calculated absorption spectra of **1** (a), **2** (b), and **3** (c) in dimethylsulfoxide.

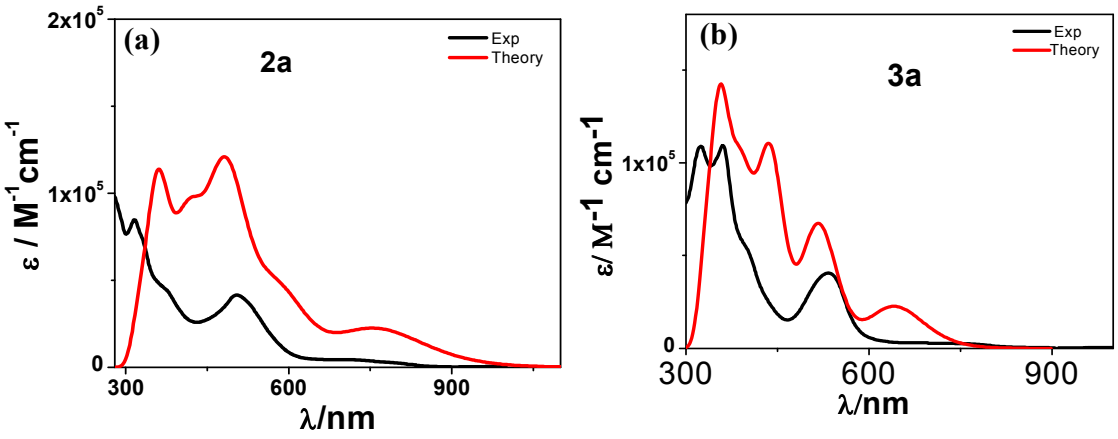

Figure S22. Experimental and calculated absorption spectra of **2a** (a) and **3a** (b) in dimethylsulfoxide.

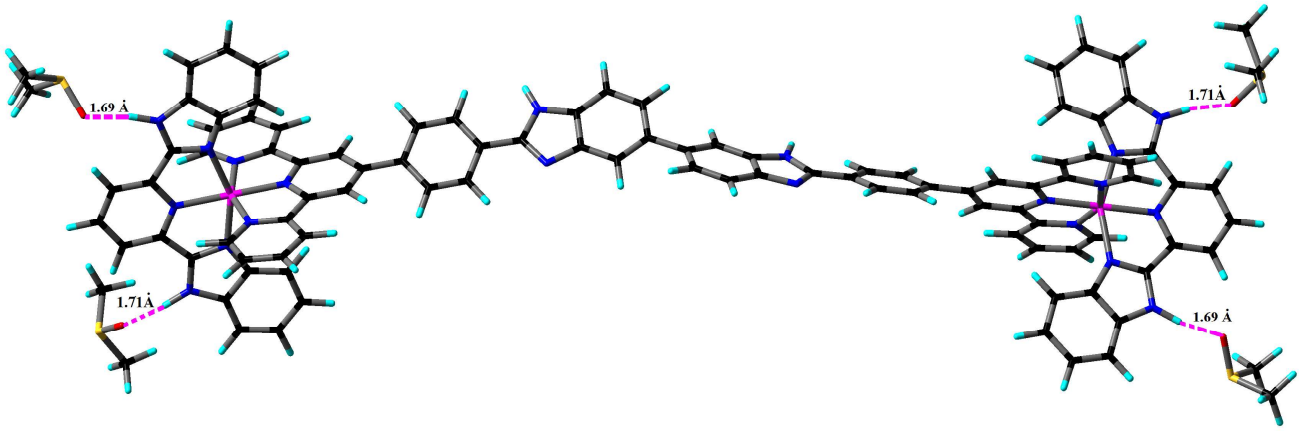

Figure S23. Hydrogen-bonded adduct for complex **3** in presence of four dimethylsulfoxide molecules.

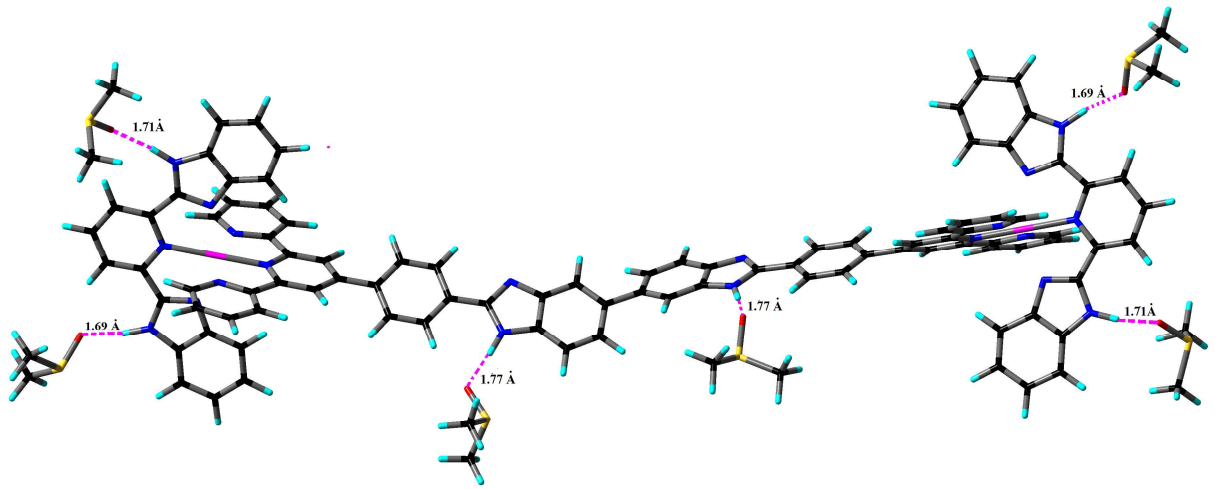

Figure S24. Hydrogen-bonded adduct for complex **3** in presence of six dimethylsulfoxide molecules.

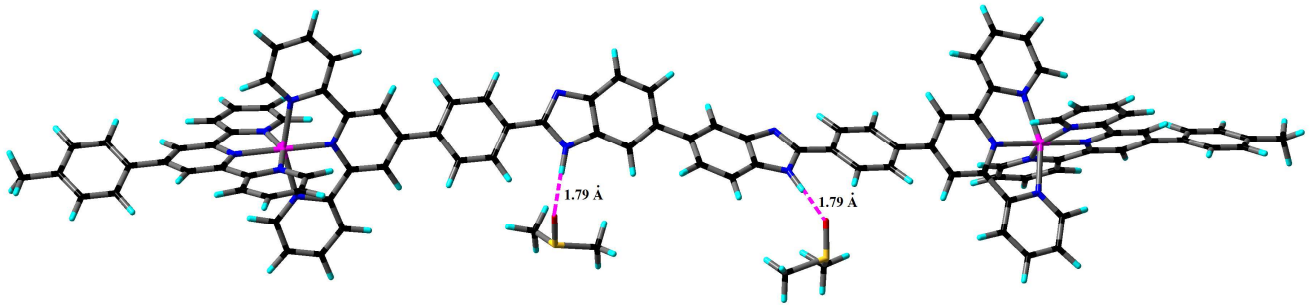

Figure S25. Hydrogen-bonded adduct for complex **1** in presence of two dimethylsulfoxide molecules.

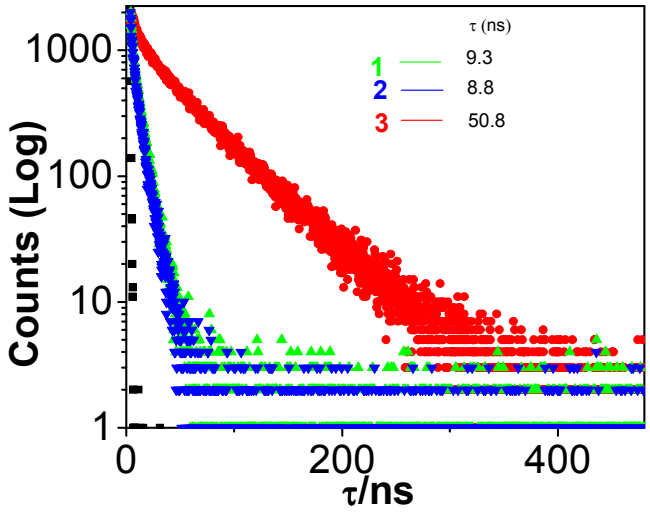

Figure S26. The excited state decay profiles for **1-3** following pulsed excitation at 450 nm in acetonitrile at room temperature. Inset shows the corresponding lifetime values.

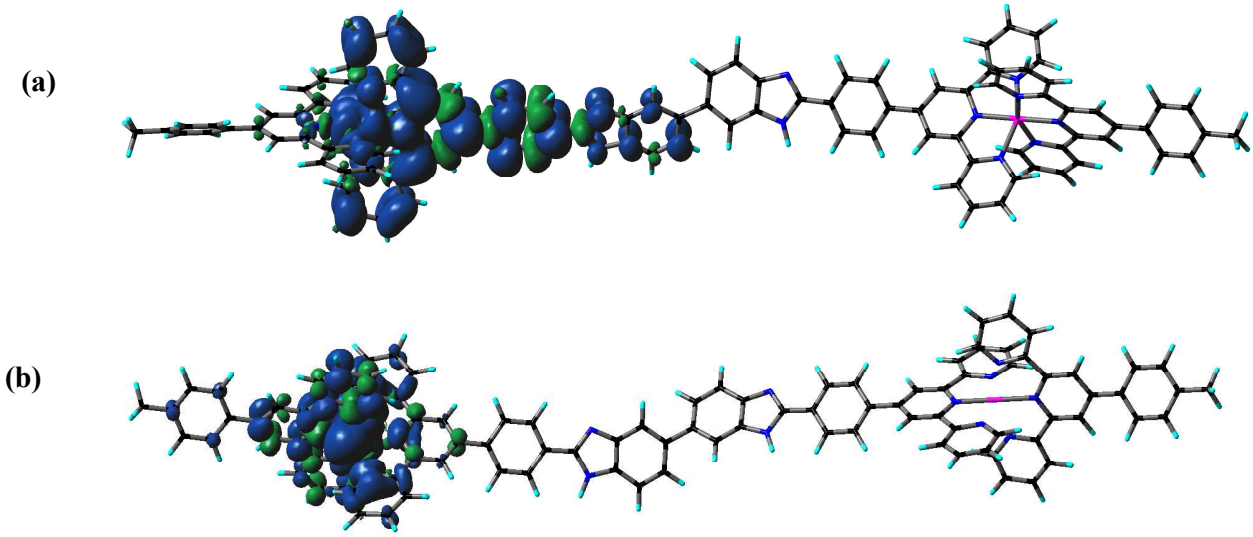

Figure S27. Spin density plots for complex **1** in ^{3}MLCT (a) and ^{3}MC (b) states.

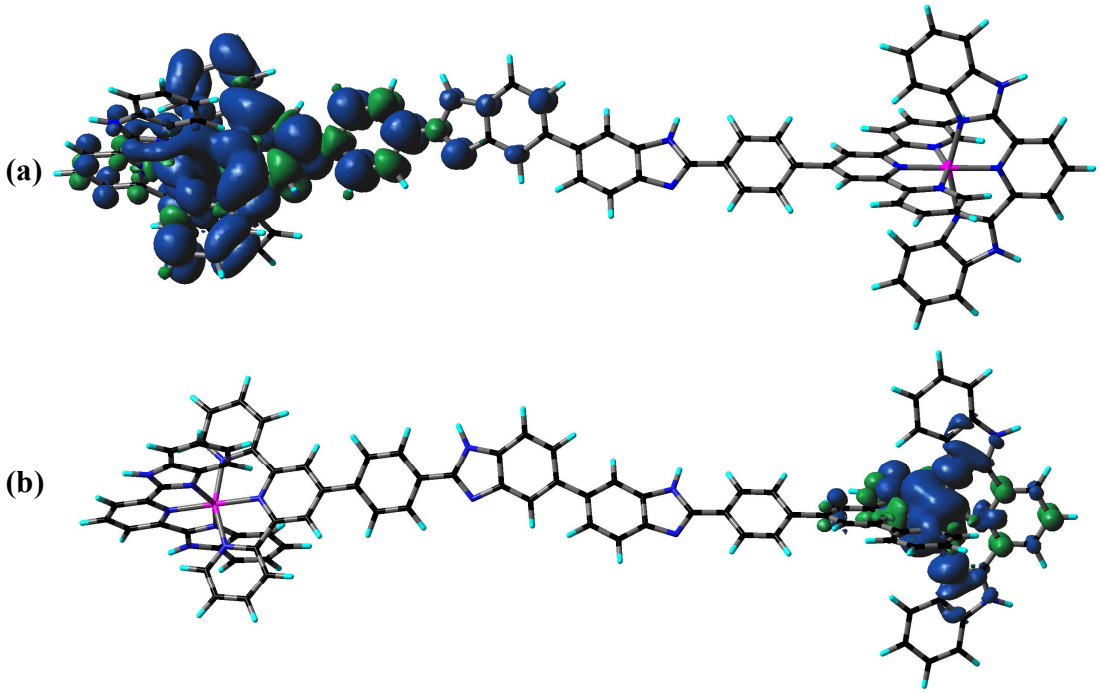

Figure S28. Spin density plots for complex **3** in ^{3}MLCT (a) and ^{3}MC (b) state.

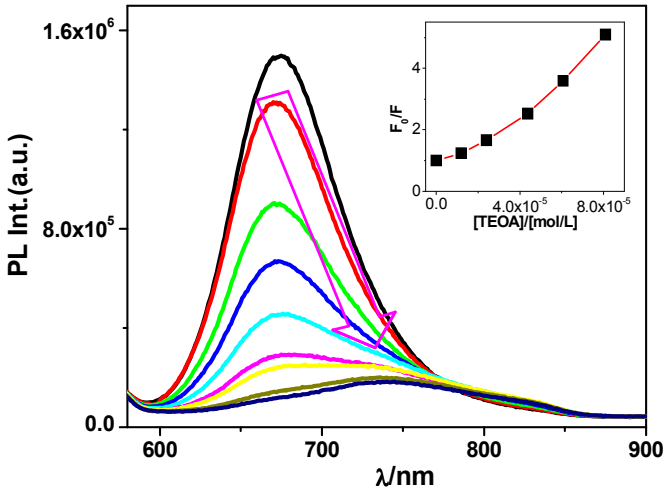

Figure S29. Emission quenching of **3** by TEOA in acetonitrile at room temperature. The excitation wavelength was 490 nm. The inset of the figure shows the Stern-Volmer plot for the emission quenching by using $F_0/F = 1 + K_{sv} \times [TEOA]$.

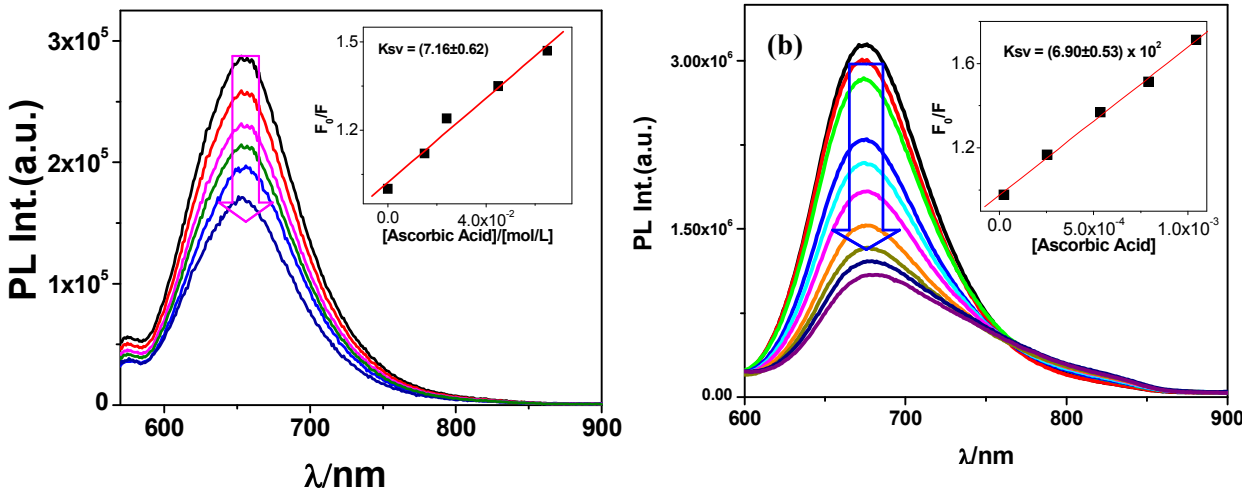

Figure S30. Emission quenching of **1** (a) and **3** (b) by ascorbic acid in acetonitrile at room temperature. The excitation wavelength was 490 nm. The inset of the figures show the Stern-Volmer plots for the emission quenching by using $F_0/F = 1 + Ksv \times$ [Asorbic Acid].

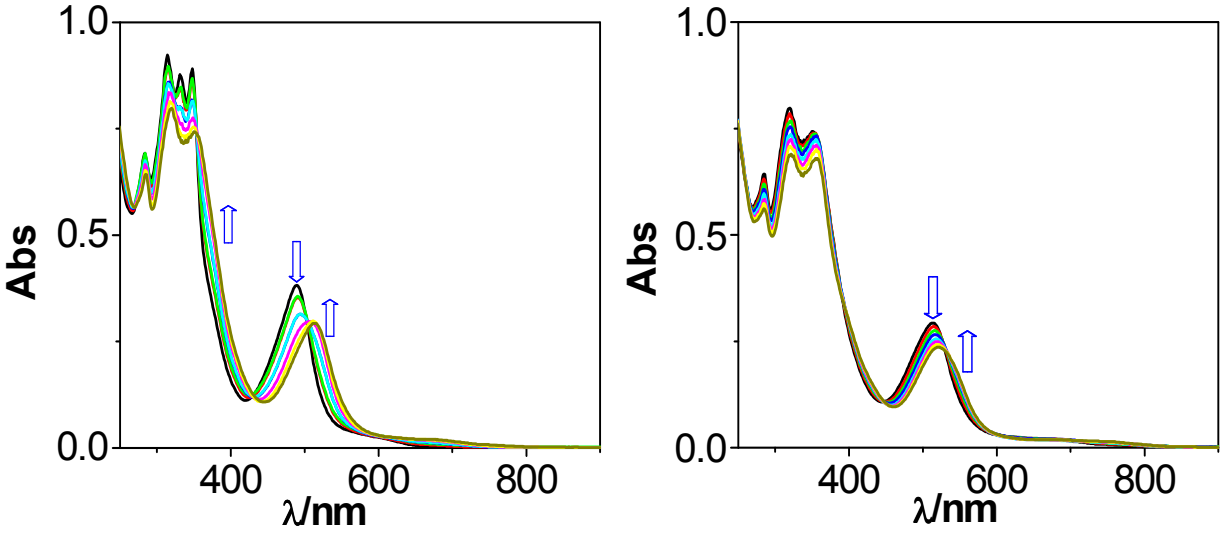

Figure S31. Two-step changes in UV-vis absorption titration of **3** upon incremental addition of TEOA in acetonitrile at room temperature.

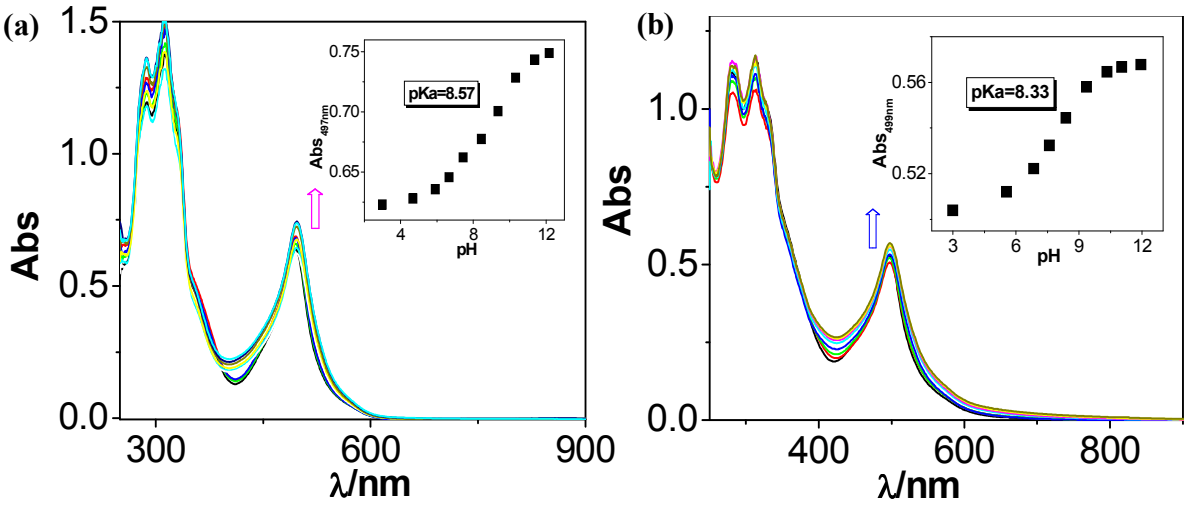

Figure S32. One-step change in the UV-vis absorption spectra of **1** (a) and **2** (b) in DMSO:H_2O (3:2 v/v) as function of pH. Insets show the variation of absorbance (at 497 nm for **1** and 499 nm for **2**) with pH as well as the pK_a values of the complexes.

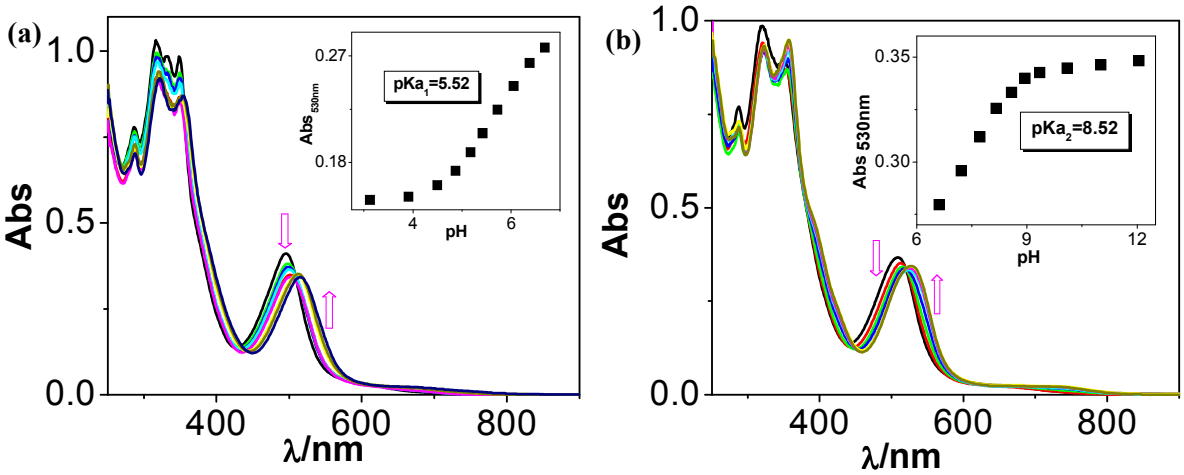

Figure S33. Two-steps changes in the UV-vis absorption spectra of **3** in DMSO:H_2O (3:2 v/v) as function of pH. Insets show the variation of absorbance at 530 nm with pH as well as the two pK_a values of the complex.

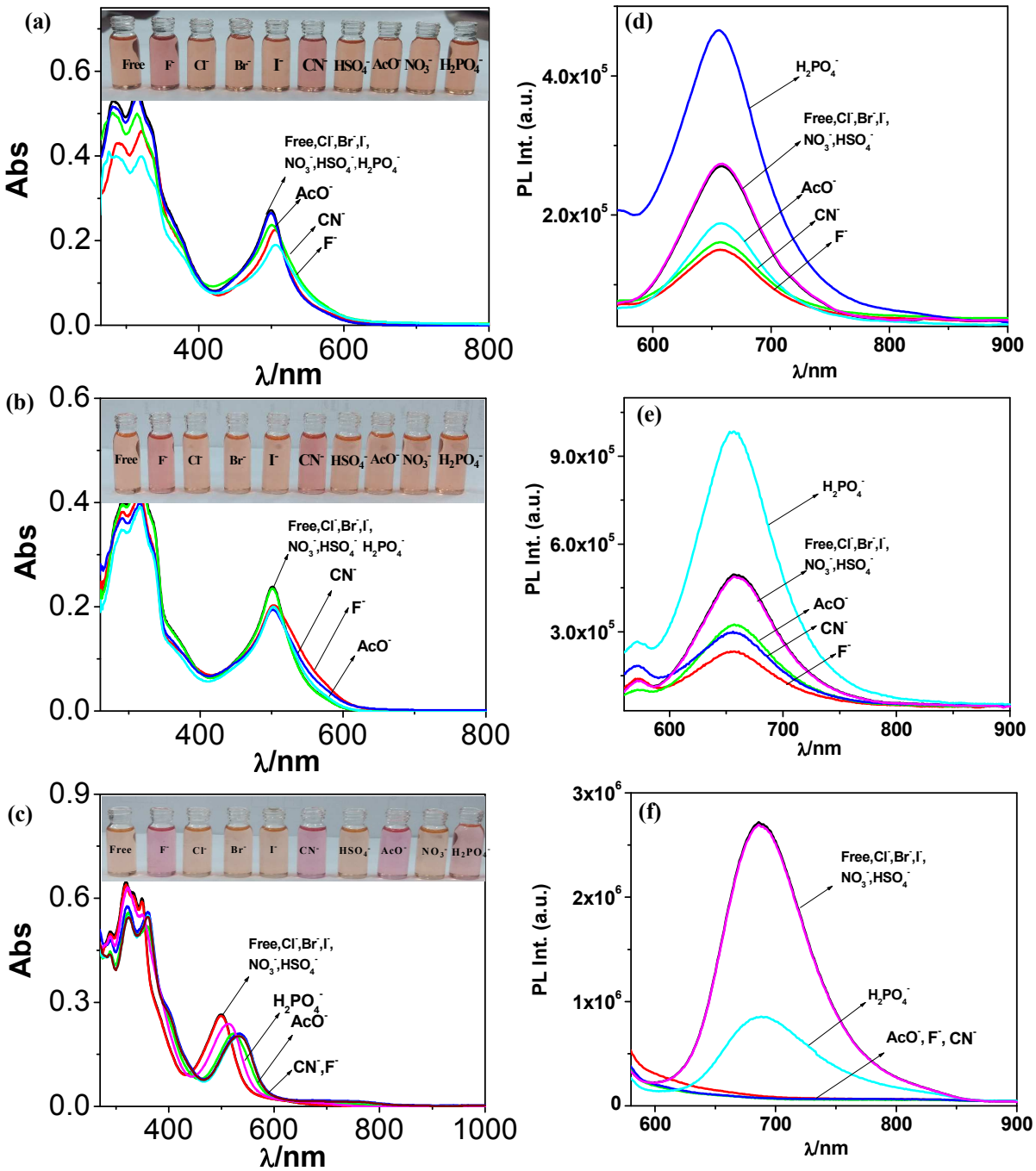

Figure S34. UV-vis absorption (a, b, and c for **1**, **2**, and **3**, respectively) and emission (d, e, and f for **1**, **2**, and **3**, respectively) spectral changes in dimethylsulfoxide upon addition of different anions as their TBA salts. Insets of (a), (b) and (c) show the visual color changes for **1**, **2** and **3**, respectively.

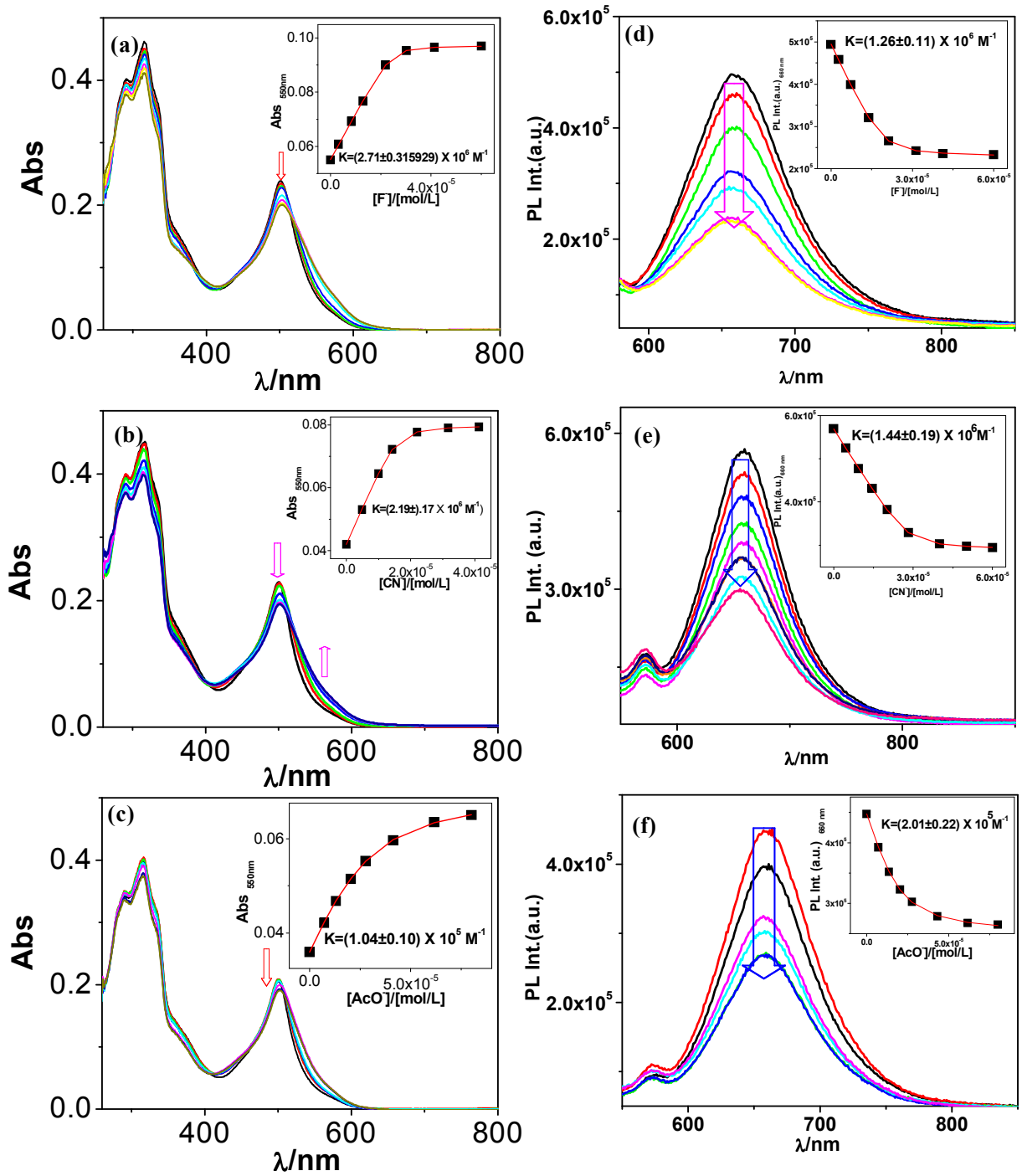

Figure S35. Changes in UV-vis absorption (a, b, and c, respectively) and luminescence (d, e, and f, respectively) spectra of **1** in dimethylsulfoxide upon incremental addition of F^-, CN^-, and AcO^-, respectively. Insets show the fit of the experimental absorbance (a-c) and luminescence (d-f) data to a 1:1 binding profile.

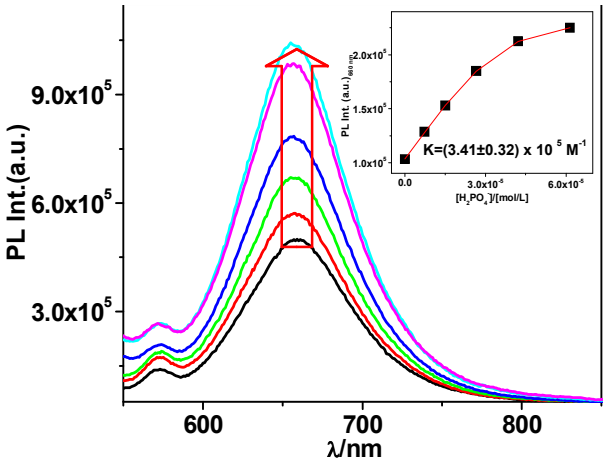

Figure 36. Steady state luminescence spectrum of **1** in dimethylsulfoxide upon incremental addition of $H_2PO_4^-$. Inset shows the fit of the experimental luminescence data to a 1:1 binding profile.

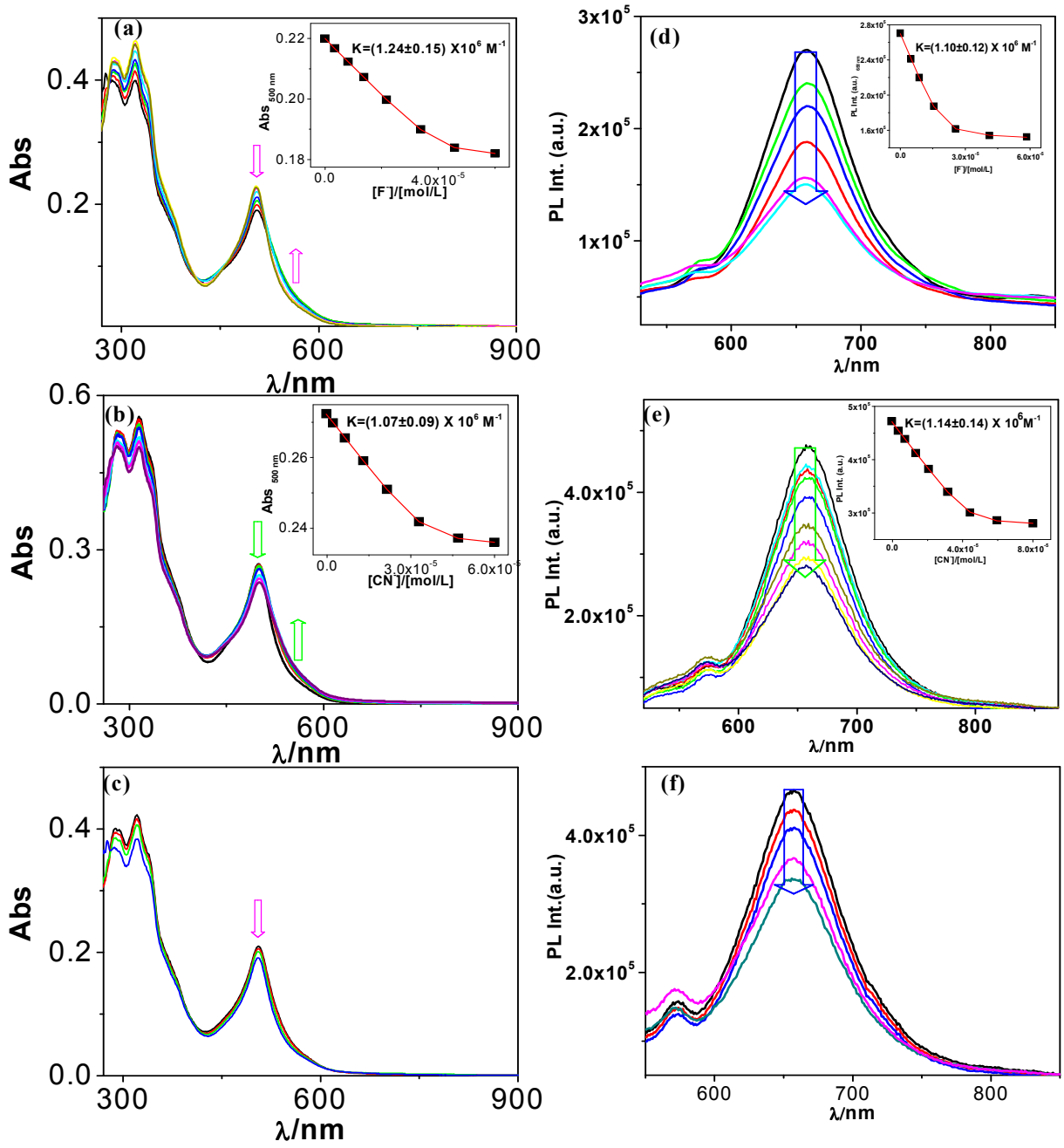

Figure S37. Changes in UV-vis absorption (a, b, and c, respectively) and luminescence (d, e, and f, respectively) spectra of **2** in dimethylsulfoxide upon incremental addition of F^-, CN^-, and AcO^-, respectively. Insets show the fit of the experimental absorbance (a and b) and luminescence (d and e) data to a 1:1 binding profile.

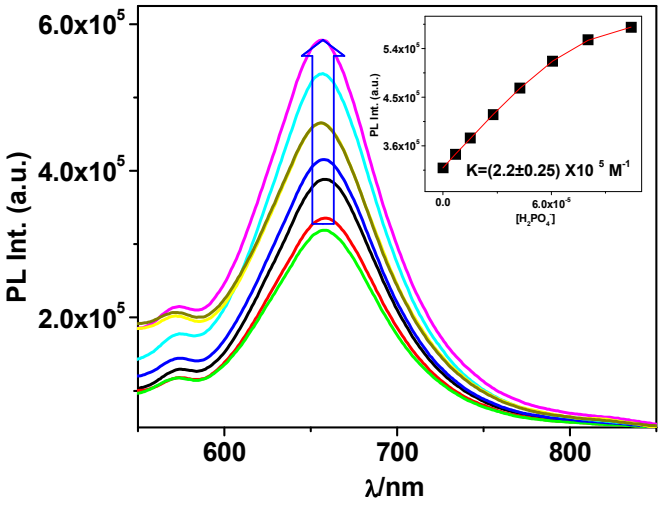

Figure S38. Changes in luminescence spectrum of **2** in dimethylsulfoxide upon incremental addition of $H_2PO_4^-$. Inset shows the fit of the experimental luminescence data to a 1:1 binding profile.

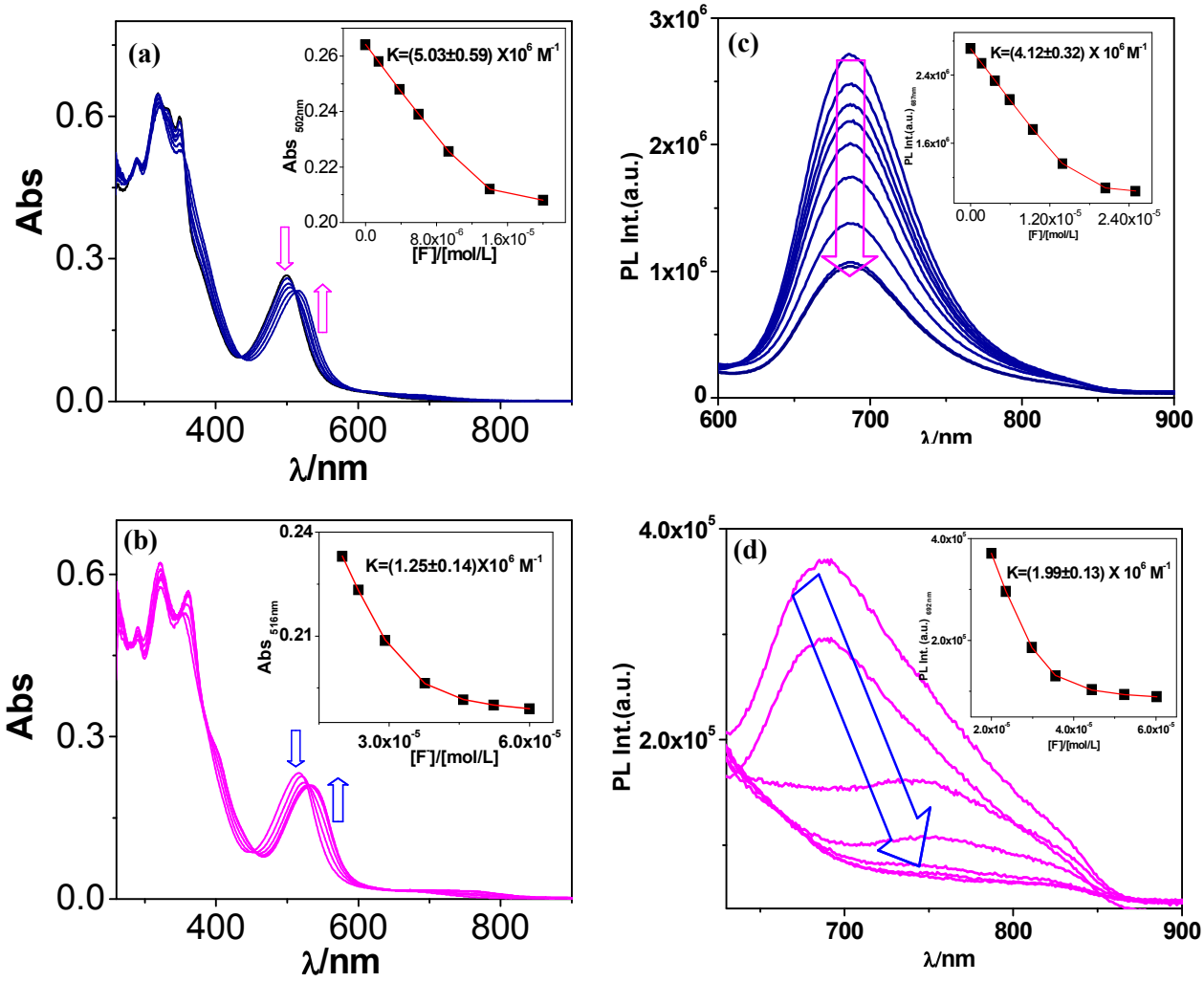

Figure S39. Changes in UV-vis absorption (a and b) and luminescence (c and d) spectra of **3** in dimethylsulfoxide upon incremental addition of F^-. Insets show the fit of the experimental absorbance (a and b) and luminescence (c and d) data to a 1:1 binding profile.

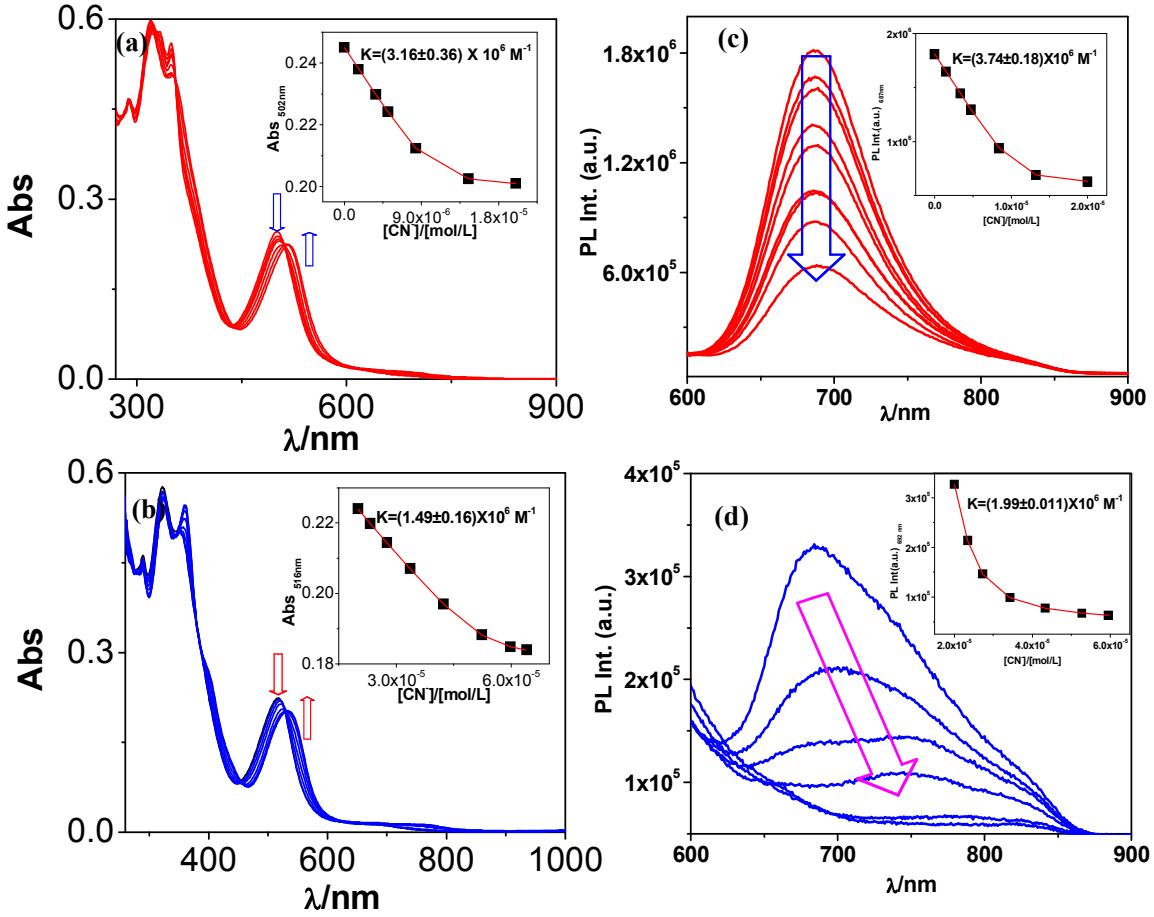

Figure S40. Changes in UV-vis absorption (a and b) and luminescence (c and d) spectra of **3** in dimethylsulfoxide upon incremental addition of CN^-. Insets show the fit of the experimental absorbance (a and b) and luminescence (c and d) data to a 1:1 binding profile.

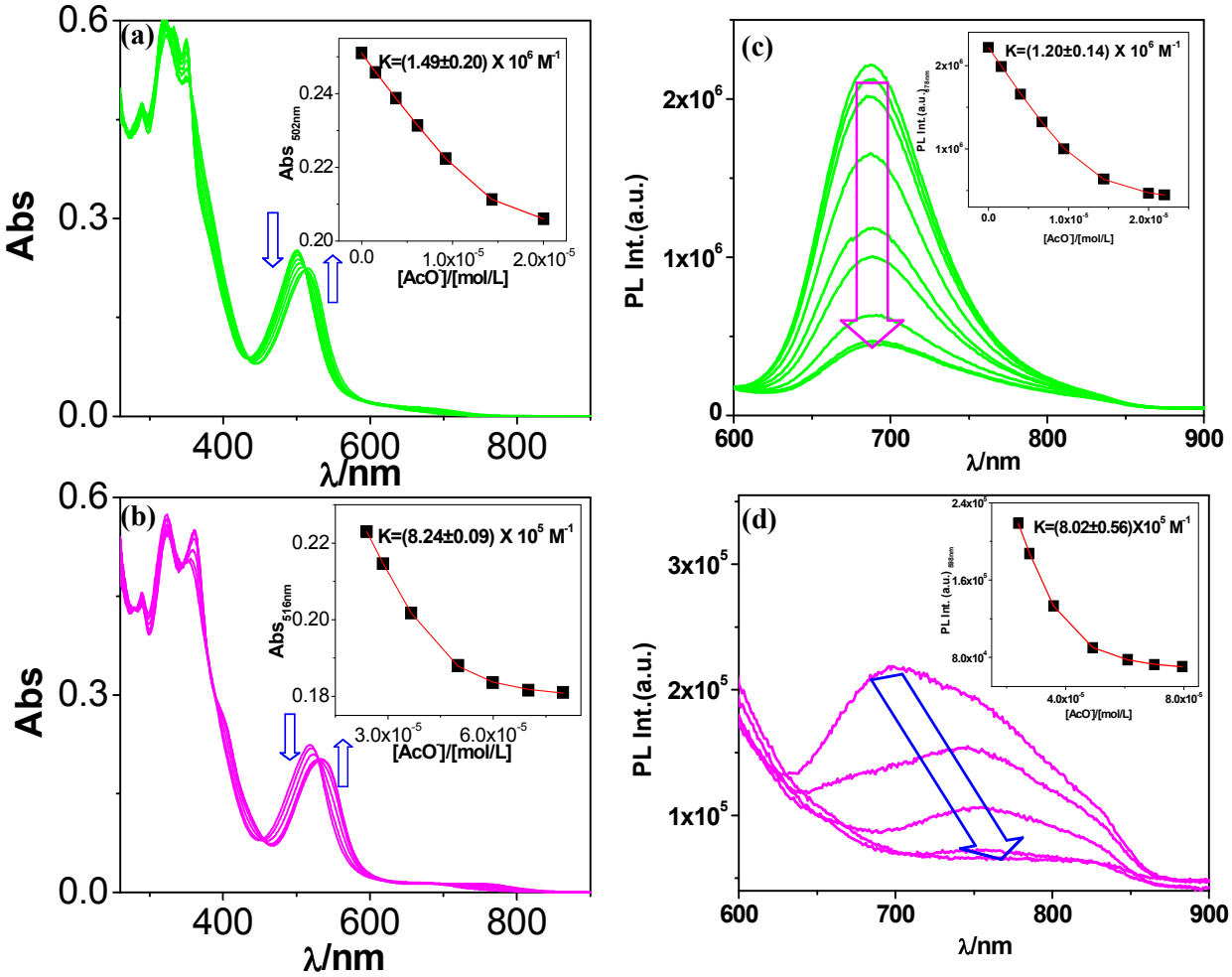

Figure S41. Changes in UV-vis absorption (a and b) and luminescence (c and d) spectra of **3** in dimethylsulfoxide upon incremental addition of AcO^-. Insets show the fit of the experimental absorbance (a and b) and luminescence (c and d) data to a 1:1 binding profile.

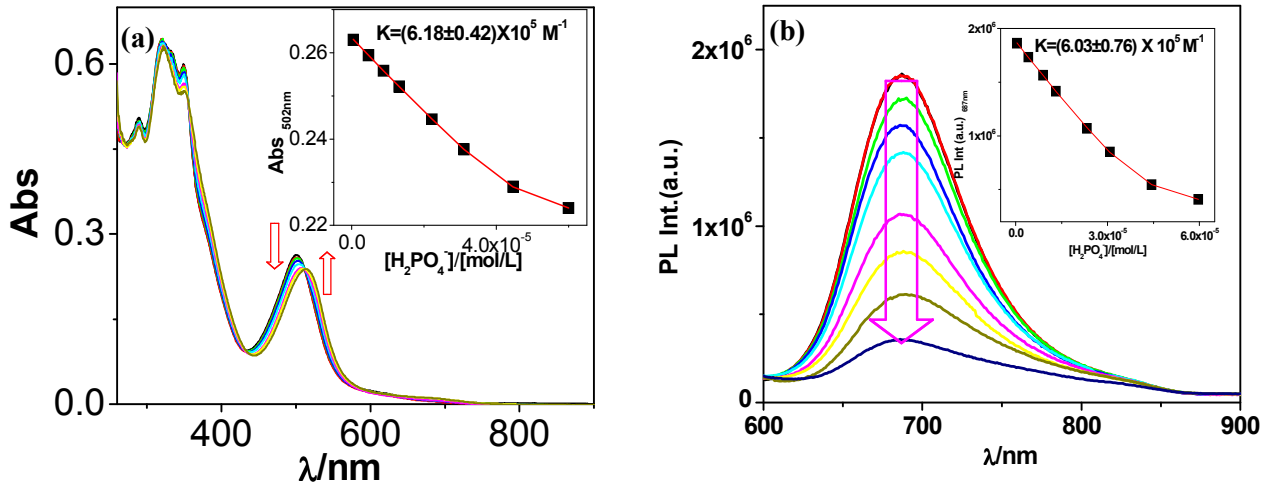

Figure S42. Changes in UV-vis absorption (a) and luminescence (b) spectra of **3** in dimethylsulfoxide upon incremental addition of $H_2PO_4^-$. Insets show the fit of the experimental absorbance (a) and luminescence (b) data to a 1:1 binding profile.

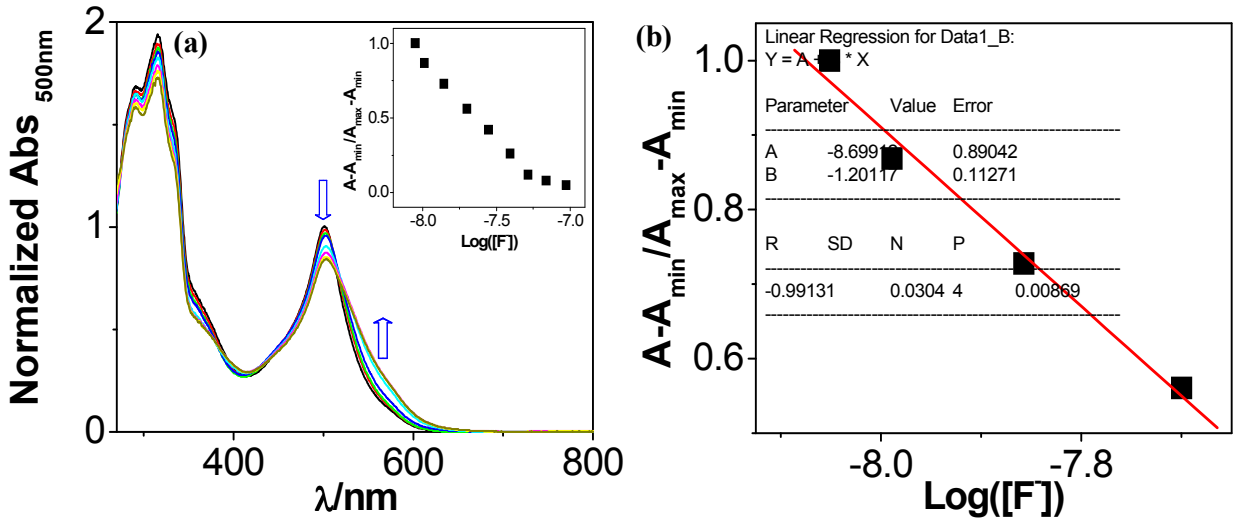

Figure S43. (a) Absorption spectral change during the titration of **1** with F^- in dimethylsulfoxide, inset shows the normalized absorbance between the minimum absorbance and the maximum absorbance. (b) A plot of $(A-A_{min})/(A_{max}-A_{min})$ vs Log([F^-]), the calculated detection limit of receptor is 3.2×10^{-9} M.

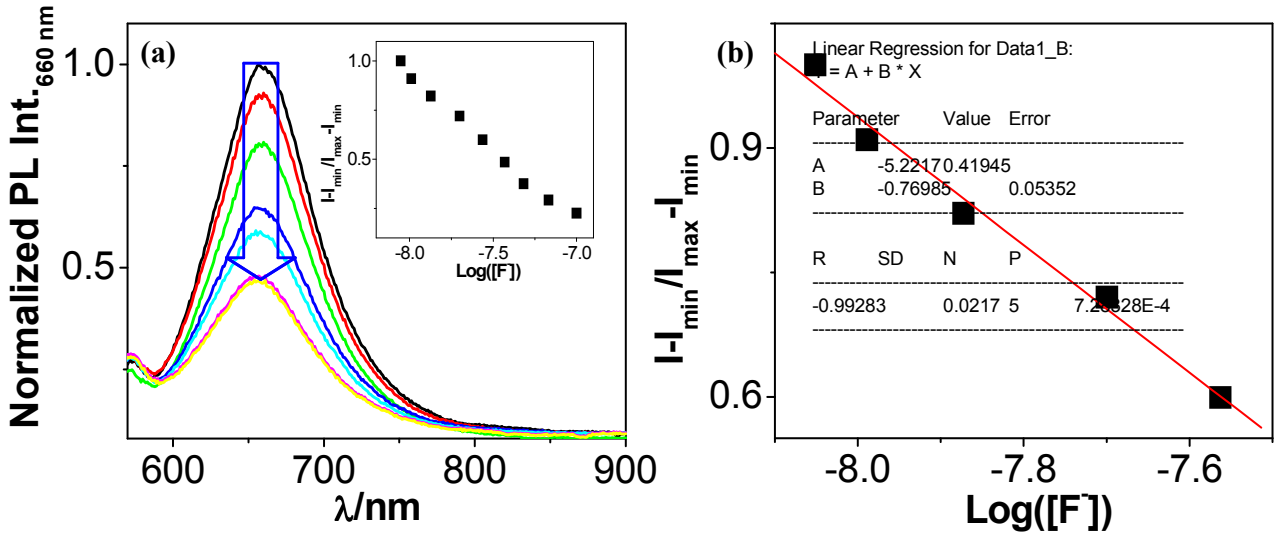

Figure S44 (a) PL spectral change during the titration of **1** with F^- in dimethylsulfoxide, inset shows the normalized intensity between the minimum intensity and the maximum intensity. (b) A plot of $(I-I_{min})/(I_{max}-I_{min})$ vs Log([F^-]), the calculated detection limit of receptor is 2.8×10^{-9} M.

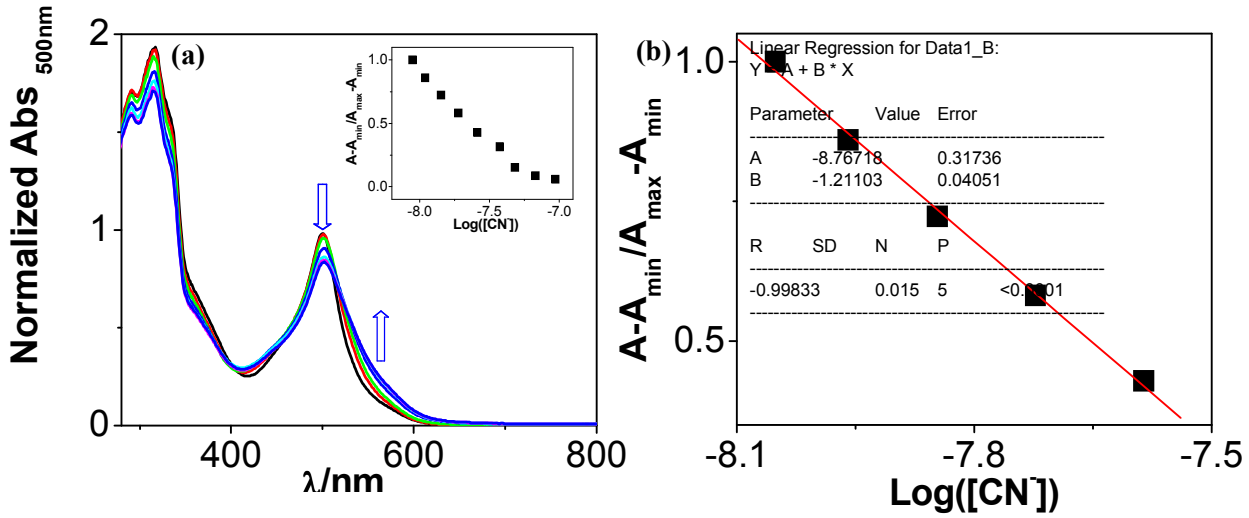

Figure S45. (a) Absorption spectral change during the titration of **1** with CN^- in dimethylsulfoxide, inset shows the normalized absorbance between the minimum absorbance and the maximum absorbance. (b) A plot of $(A-A_{min})/(A_{max}-A_{min})$ vs $Log([CN^-])$, the calculated detection limit of receptor is 5.1×10^{-9} M.

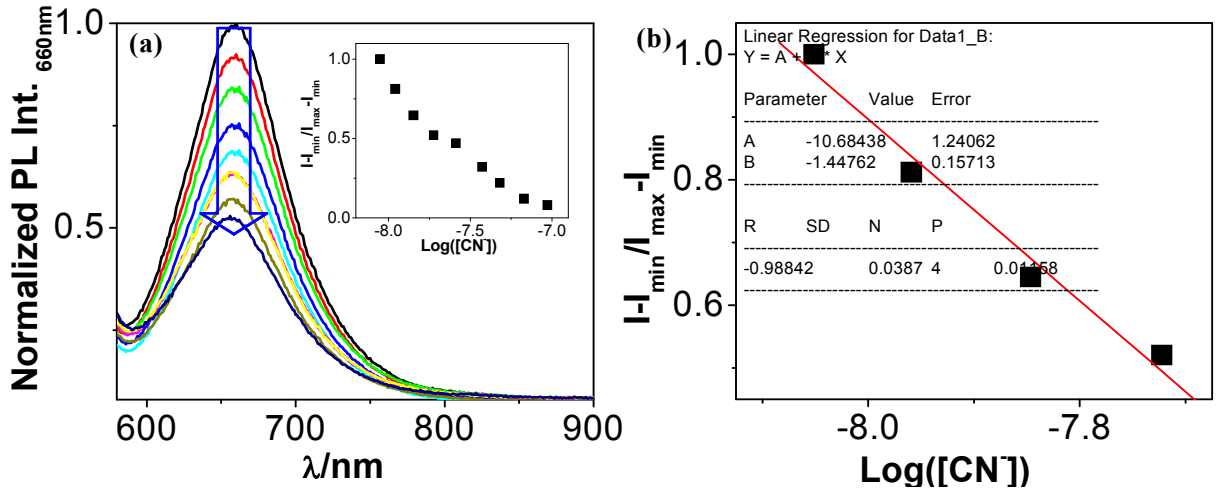

Figure S46. (a) PL spectral change during the titration of **1** with CN^- in dimethylsulfoxide, inset shows the normalized intensity between the minimum intensity and the maximum intensity. (b) A plot of $(I-I_{min})/(I_{max}-I_{min})$ vs $Log([CN^-])$, the calculated detection limit of receptor is 6.4×10^{-9} M.

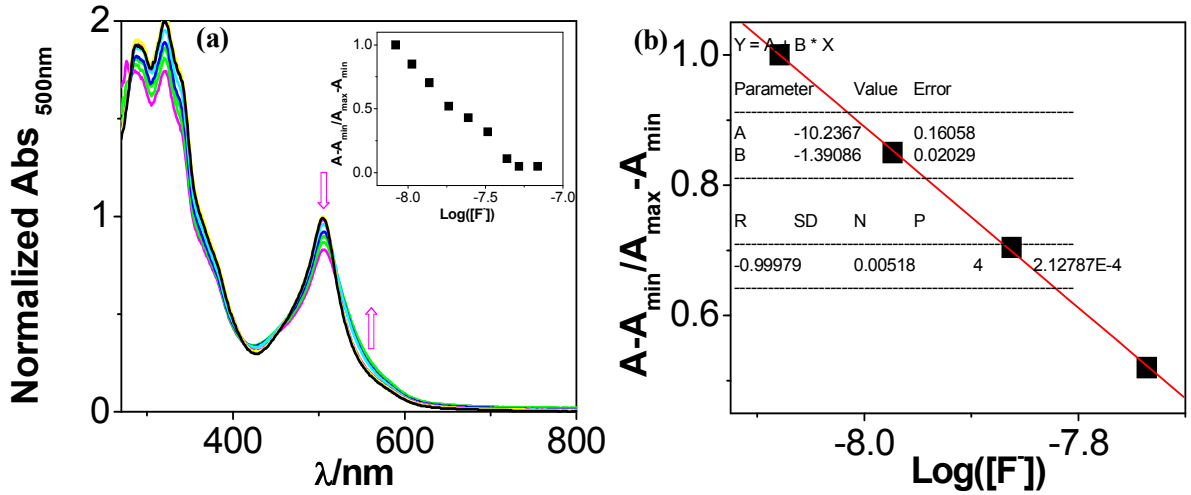

Figure S47. (a) Absorption spectral change during the titration of **2** with F^- in dimethylsulfoxide, inset shows the normalized absorbance between the minimum absorbance and the maximum absorbance. (b) A plot of $(A-A_{min})/(A_{max}-A_{min})$ vs $Log([F^-])$, the calculated detection limit of receptor is 2.4×10^{-9} M.

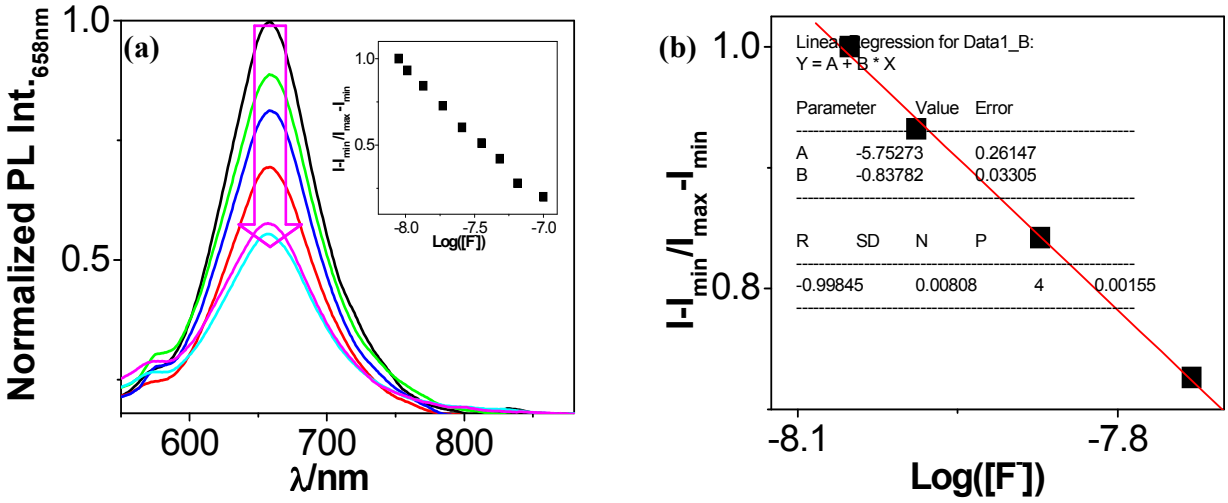

Figure S48. (a) PL spectral change during the titration of **2** with F^- in dimethylsulfoxide, inset shows the normalized intensity between the minimum intensity and the maximum intensity. (b) A plot of $(I-I_{min})/(I_{max}-I_{min})$ vs $Log([F^-])$, the calculated detection limit of receptor is 2.07×10^{-9} M.

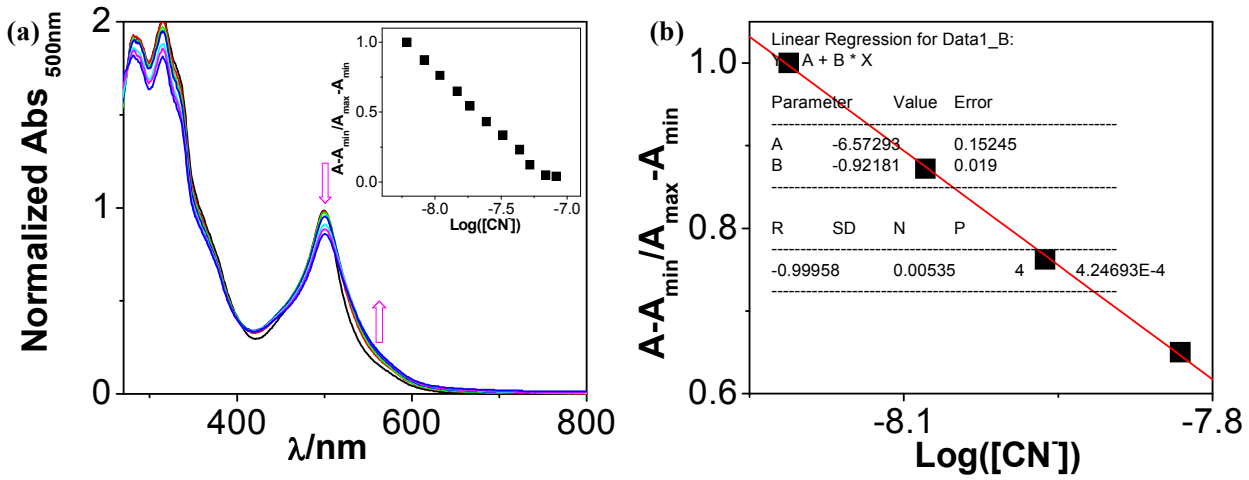

Figure S49. (a) Absorption spectral change during the titration of **2** with CN^- in dimethylsulfoxide, inset shows the normalized absorbance between the minimum absorbance and the maximum absorbance. (b) A plot of $(A-A_{min})/(A_{max}-A_{min})$ vs $Log([CN^-])$, the calculated detection limit of receptor is 5.0×10^{-9} M.

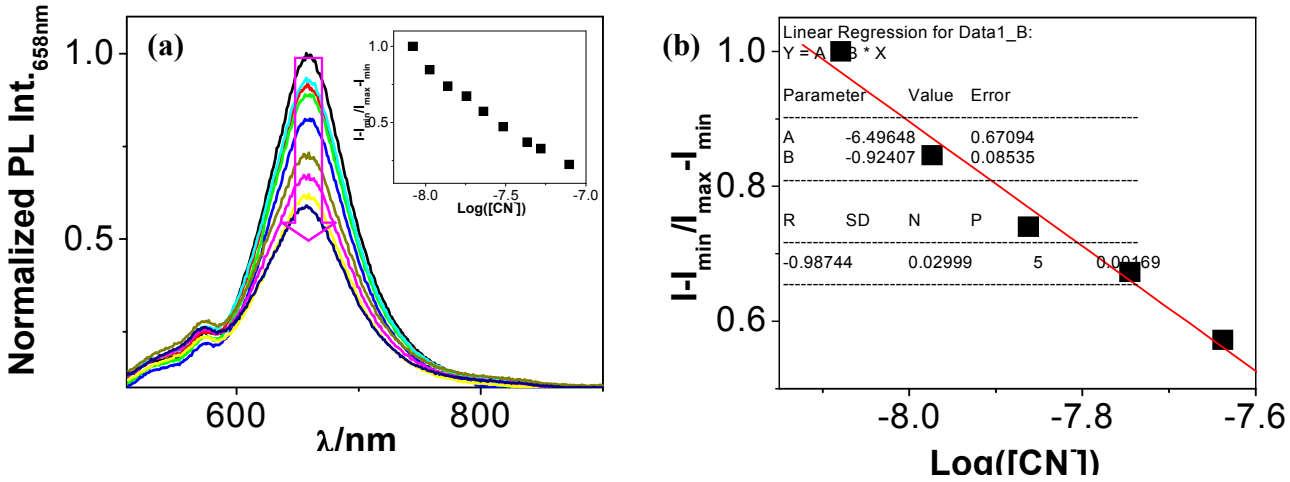

Figure S50. (a) PL spectral change during the titration of **2** with CN^- in dimethylsulfoxide, inset shows the normalized intensity between the minimum intensity and the maximum intensity. (b) A plot of $(I-I_{min})/(I_{max}-I_{min})$ vs $Log([CN^-])$, the calculated detection limit of receptor is 5.3×10^{-9} M.

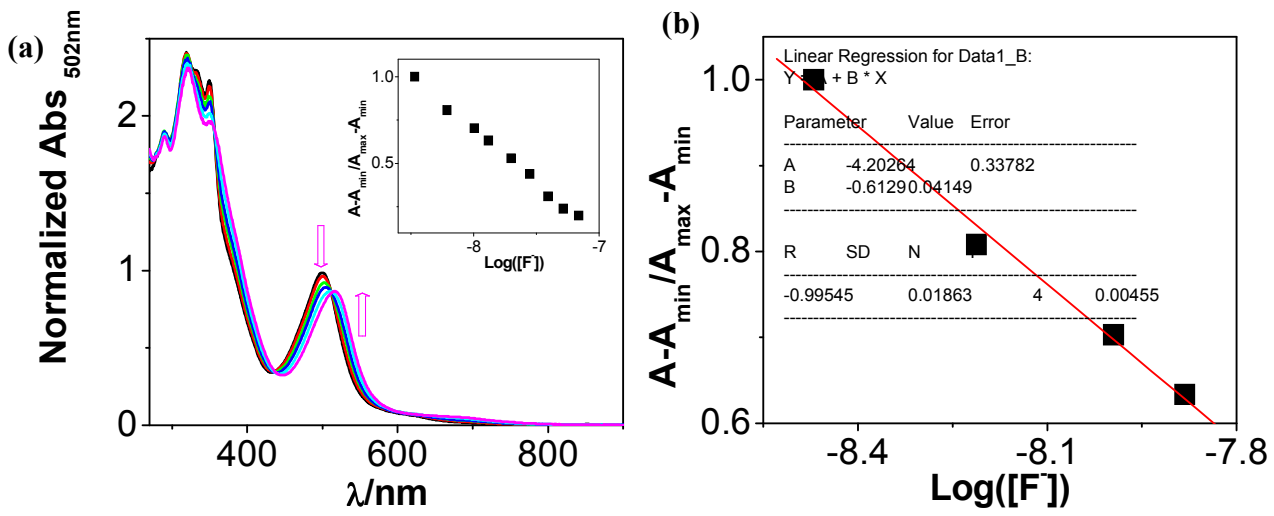

Figure S51. (a) Absorption spectral change during the titration of **3** with F^- in dimethylsulfoxide, inset shows the normalized absorbance between the minimum absorbance and the maximum absorbance. (b) A plot of $(A-A_{min})/(A_{max}-A_{min})$ vs $Log([F^-])$, the calculated detection limit of receptor is 1.8×10^{-9} M.

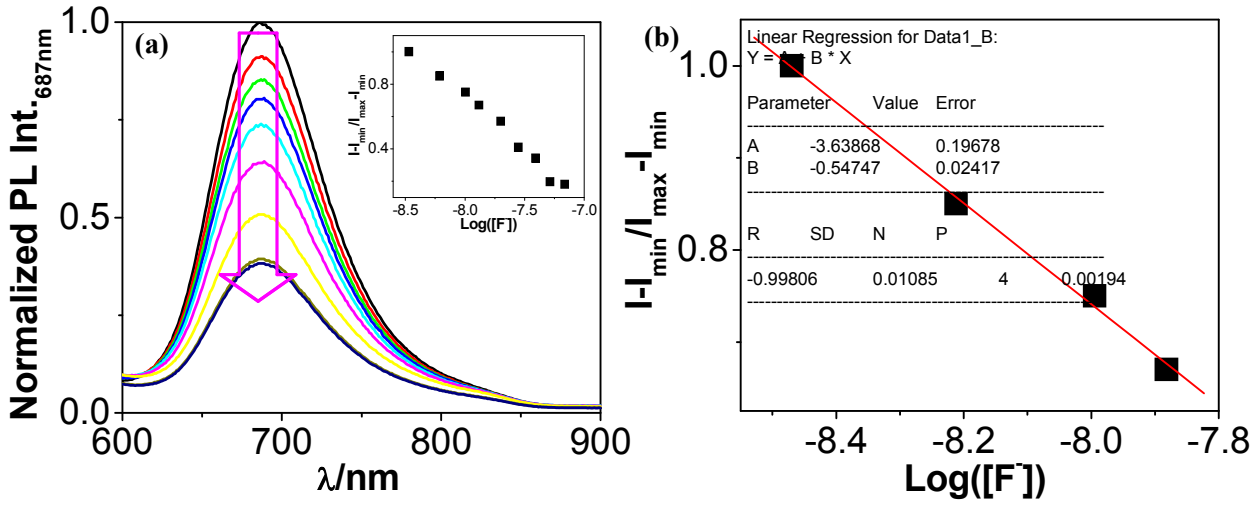

Figure S52. **(a)** PL spectral change during the titration of **3** with F^- in dimethylsulfoxide, inset shows the normalized intensity between the minimum intensity and the maximum intensity. (b) A plot of $(I-I_{min})/(I_{max}-I_{min})$ vs $Log([F^-])$, the calculated detection limit of receptor is 1.7×10^{-9} M.

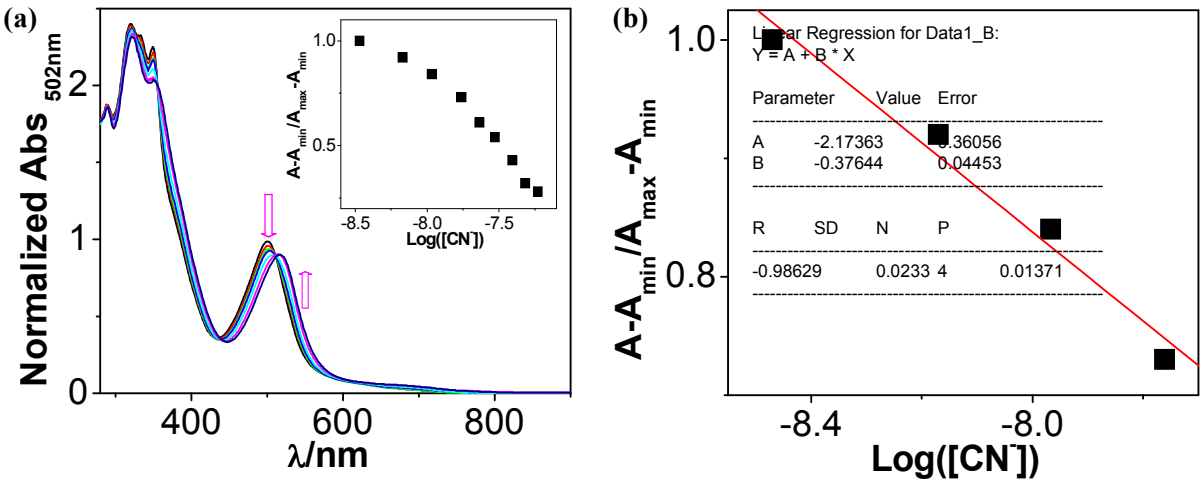

Figure S53. (a) Absorption spectral change during the titration of **3** with CN^- in dimethylsulfoxide, inset shows the normalized absorbance between the minimum absorbance and the maximum absorbance. (b) A plot of $(A-A_{min})/(A_{max}-A_{min})$ vs $Log([CN^-])$, the calculated detection limit of receptor is 2.3×10^{-9} M.

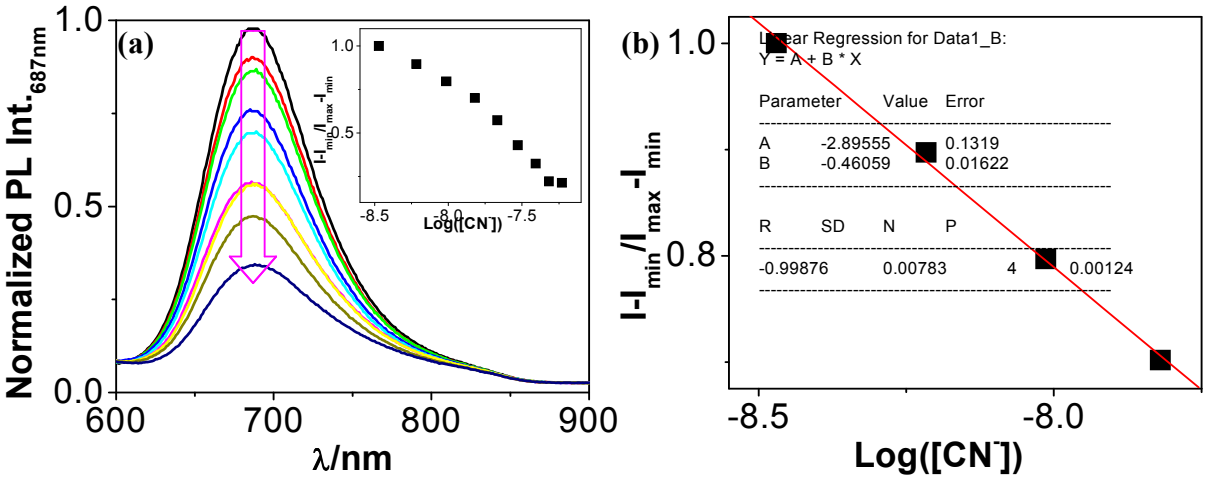

Figure S54. (a) PL spectral change during the titration of **3** with CN^- in dimethylsulfoxide, inset shows the normalized intensity between the minimum intensity and the maximum intensity. (b) A plot of $(I-I_{min})/(I_{max}-I_{min})$ vs $Log([CN^-])$, the calculated detection limit of receptor is 2.5×10^{-9} M.

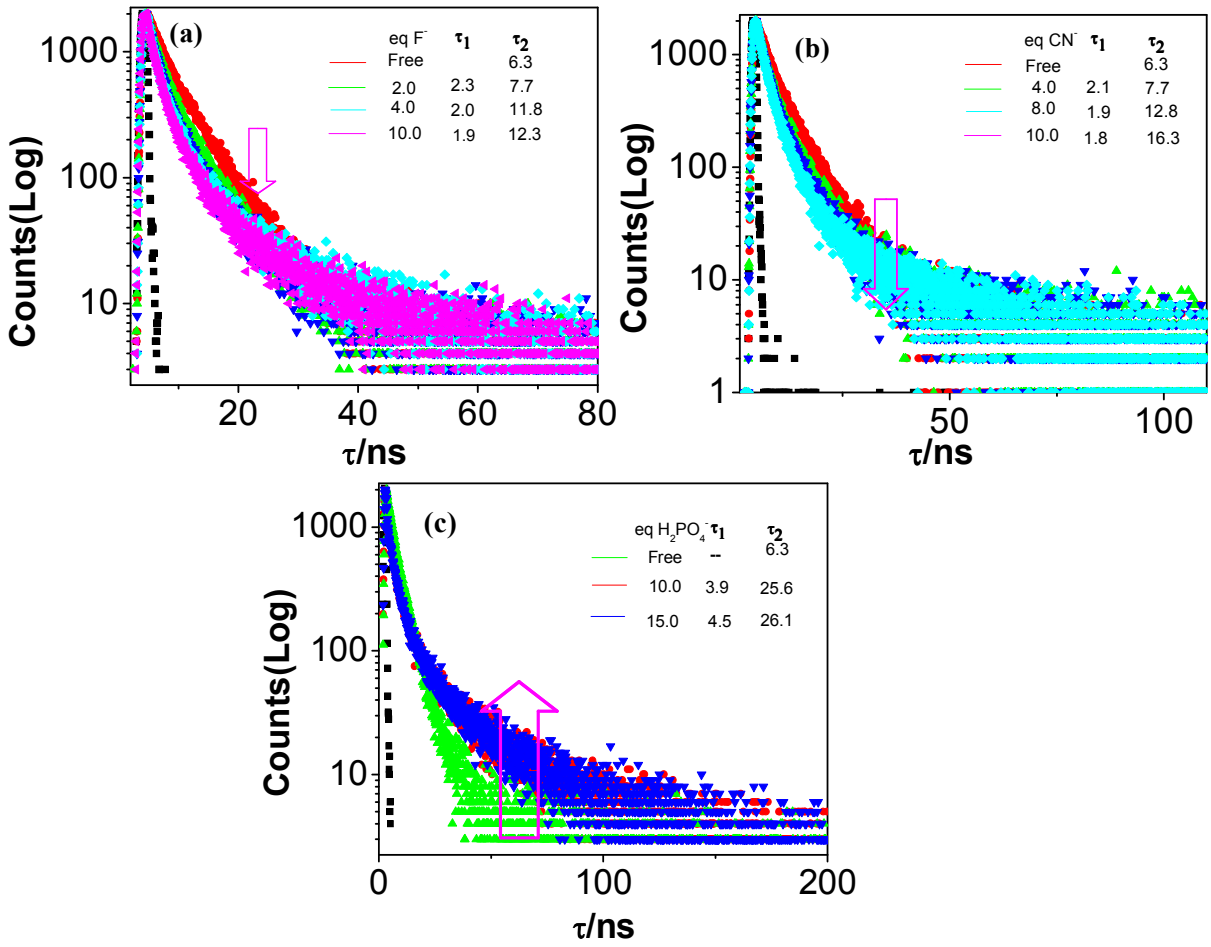

Figure S55. Changes in excited state decay profile of **1** in dimethylsulfoxide upon incremental addition of F^- (a), CN^- (b) and $H_2PO_4^-$(c). Insets shows the corresponding lifetime values.

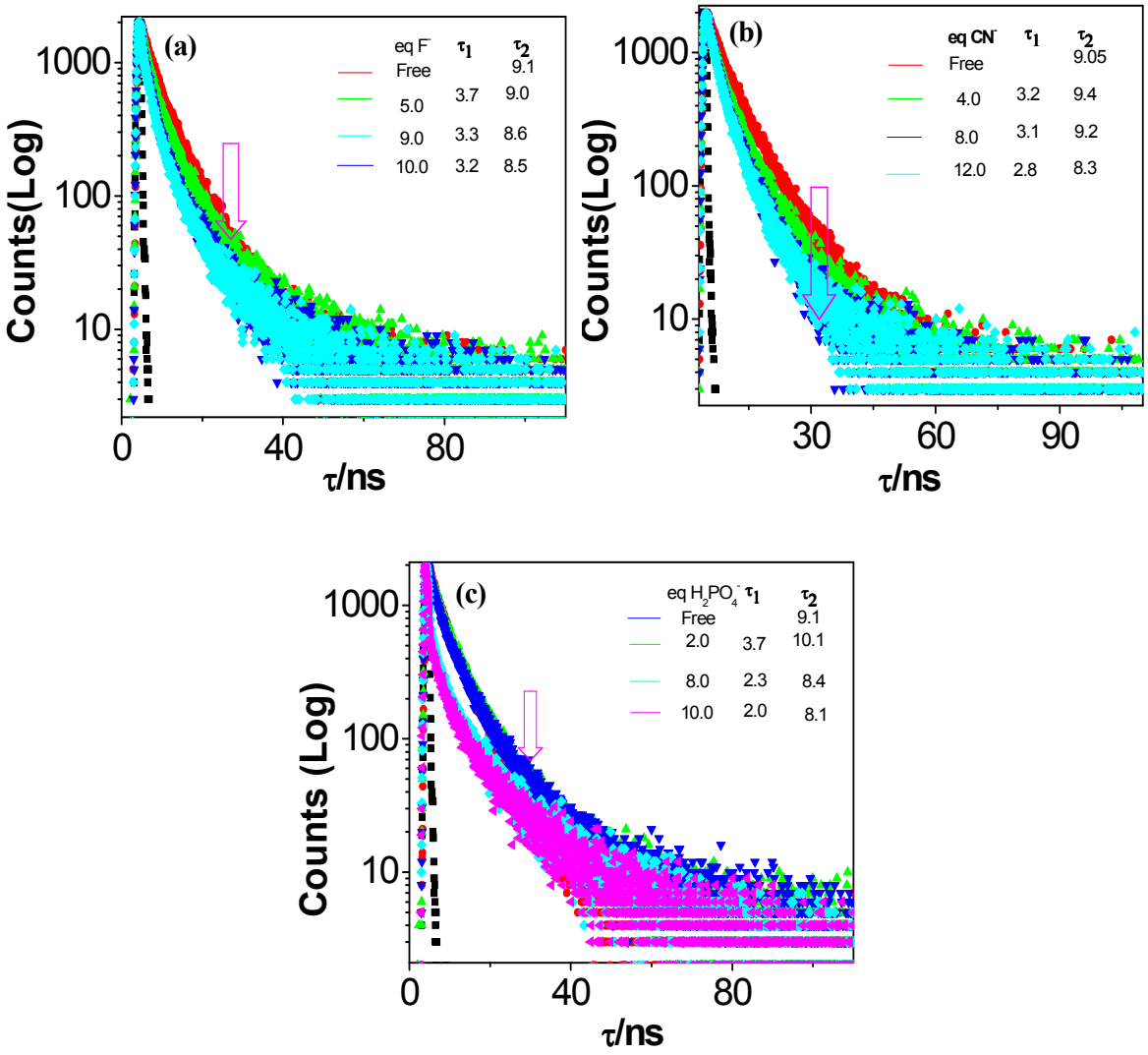

Figure S56. Changes in the excited state decay profile of **2** in dimethylsulfoxide upon incremental addition of F^- (a), CN^- (b), and $H_2PO_4^-$(c). Insets show the corresponding lifetime values.

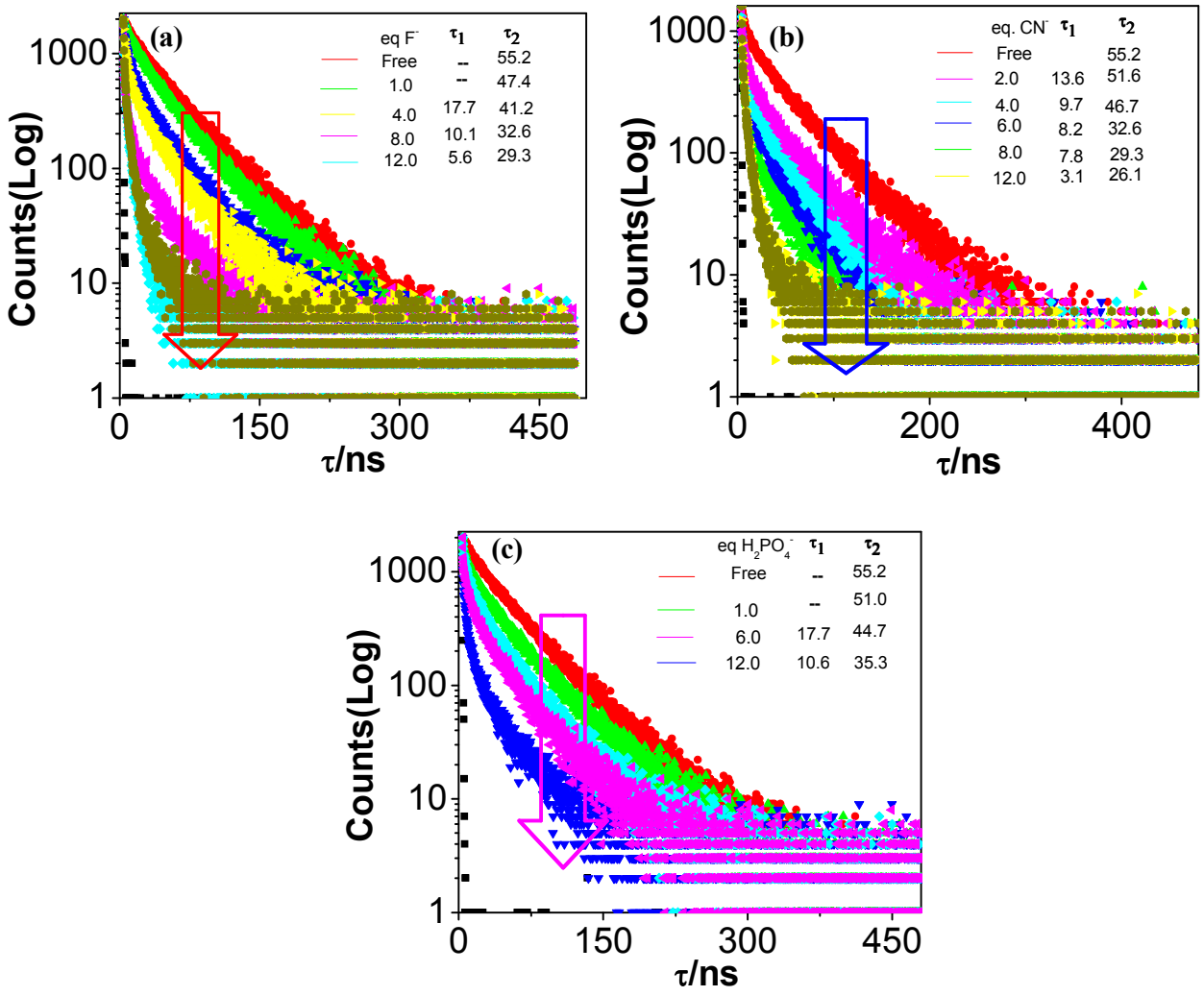

Figure S57. Changes in excited state decay profiles of **3** in dimethylsulfoxide upon incremental addition of F^- (a), CN^- (b) and $H_2PO_4^-$ (c). Insets show the corresponding lifetime values.

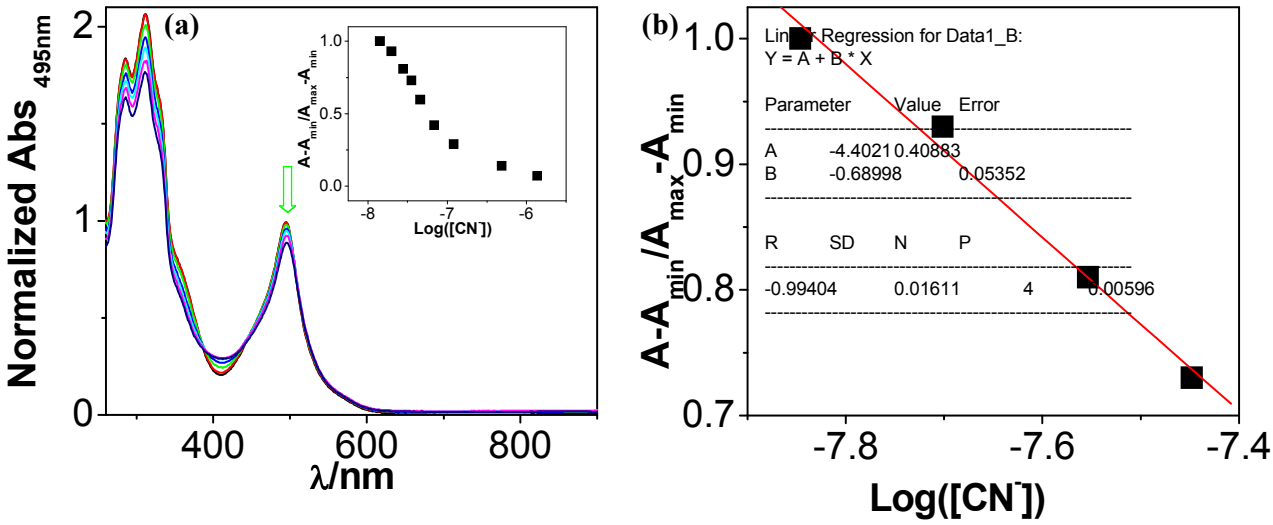

Figure S58. (a) Absorption spectral change during the titration of **1** with CN^- in water:dimethylsulfoxide (100:1, v/v), inset shows the normalized absorbance between the minimum absorbance and the maximum absorbance. (b) A plot of $(A-A_{min})/(A_{max}-A_{min})$ vs $Log([CN^-])$, the calculated detection limit of receptor is 4.2×10^{-8} M.

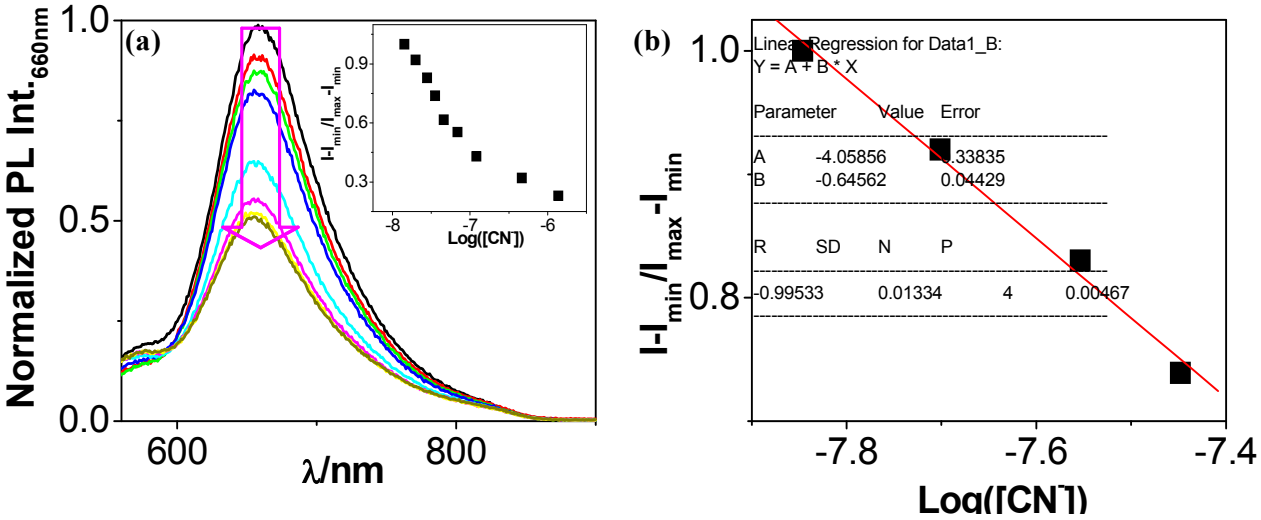

Figure S59. (a) PL spectral change during the titration of **1** with CN^- in water:dimethylsulfoxide(100:1, v/v), inset shows the normalized intensity between the minimum intensity and the maximum intensity. (b) A plot of $(I-I_{min})/(I_{max}-I_{min})$ vs $Log([CN^-])$, the calculated detection limit of receptor is 4.07×10^{-8} M.

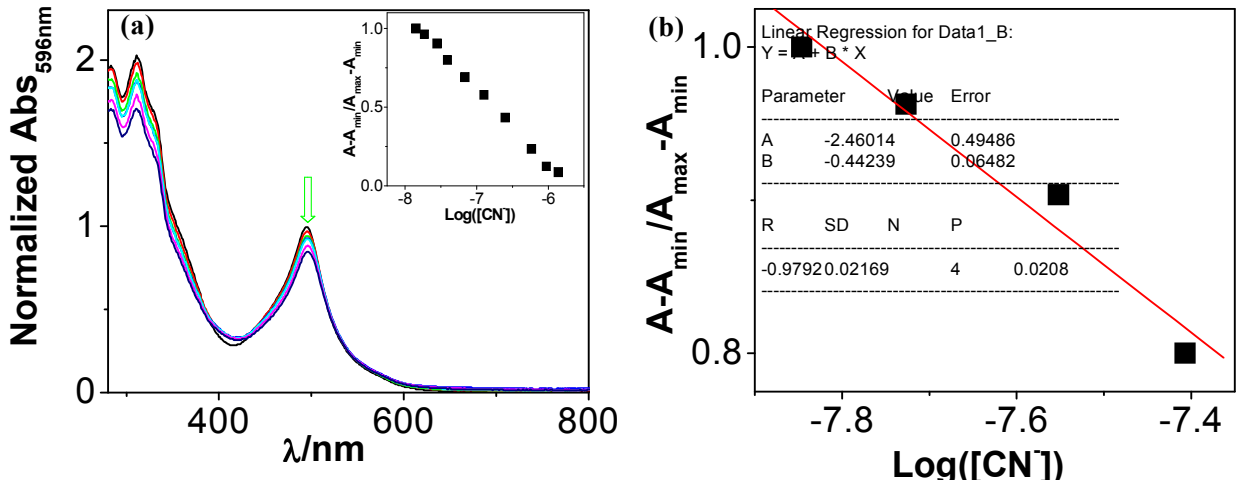

Figure S60. (a) Absorption spectral change during the titration of **2** with CN^- in water:dimethylsulfoxide (100:1, v/v), inset shows the normalized absorbance between the minimum absorbance and the maximum absorbance. (b) A plot of $(A-A_{min})/(A_{max}-A_{min})$ vs $Log([CN^-])$, the calculated detection limit of receptor is 6.3×10^{-8} M.

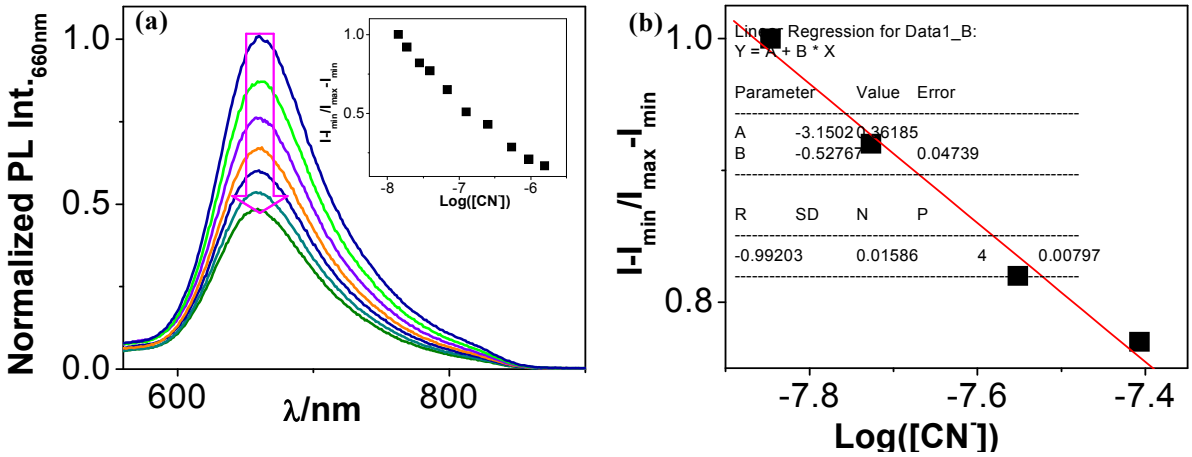

Figure S61. (a) PL spectral change during the titration of **2** with CN^- in water: dimethylsulfoxide (100:1, v/v), inset shows the normalized intensity between the minimum intensity and the maximum intensity. (b) A plot of $(I-I_{min})/(I_{max}-I_{min})$ vs $Log([CN^-])$, the calculated detection limit of receptor is 6.4×10^{-8} M.

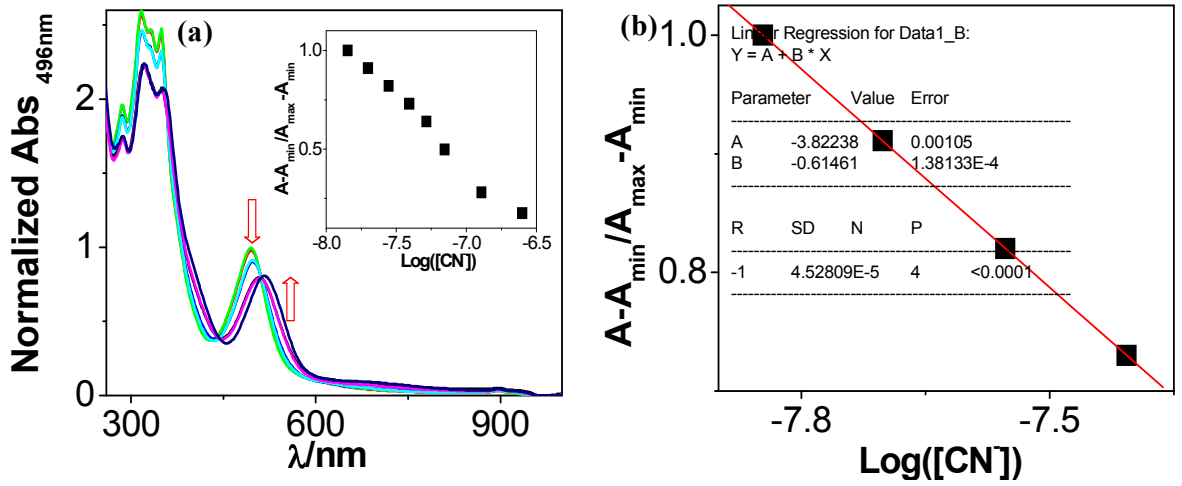

Figure S62. (a) Absorption spectral change during the titration of **3** with CN^- in water:dimethylsulfoxide (100:1, v/v), inset shows the normalized absorbance between the minimum absorbance and the maximum absorbance. (b) A plot of $(A-A_{min})/(A_{max}-A_{min})$ vs $Log([CN^-])$, the calculated detection limit of receptor is 2.5×10^{-8} M.

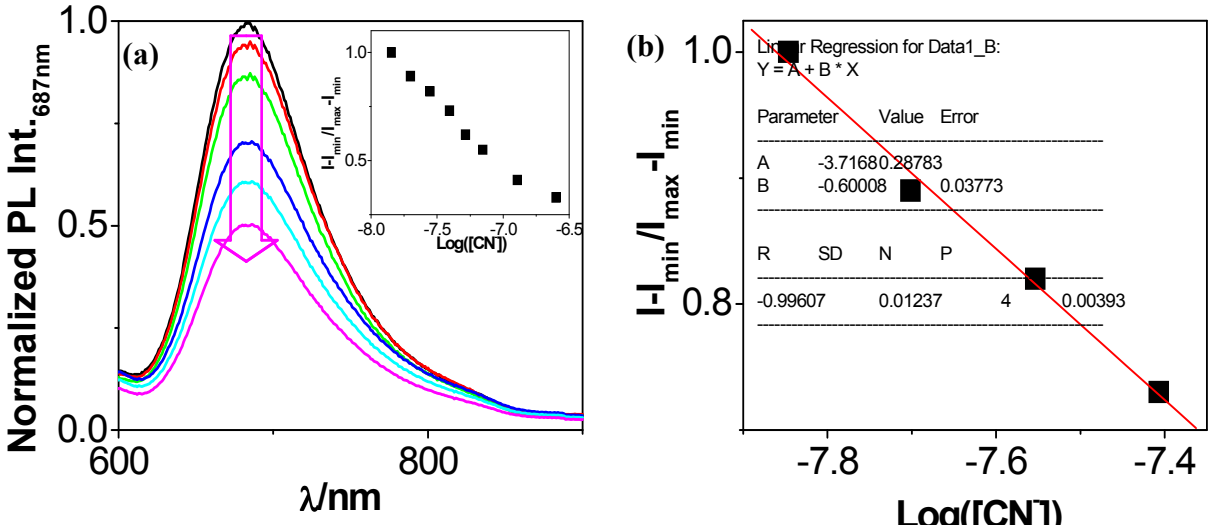

Figure S63. (a) PL spectral change during the titration of **3** with CN^- in water:dimethylsulfoxide (100:1, v/v), inset shows the normalized intensity between the minimum intensity and the maximum intensity. (b) A plot of $(I-I_{min})/(I_{max}-I_{min})$ vs $Log([CN^-])$, the calculated detection limit of receptor is 2.41×10^{-8} M.

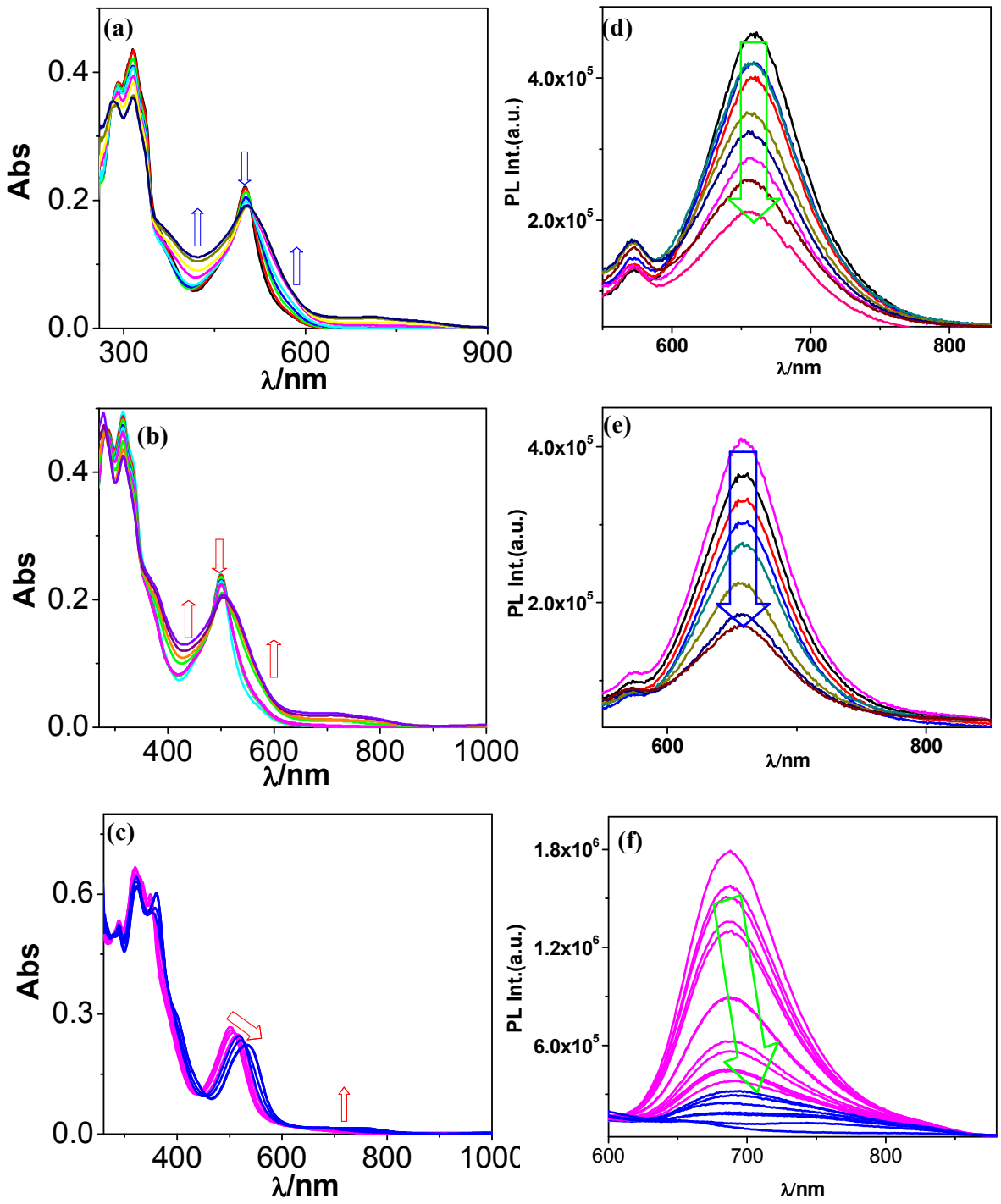

Figure S64. Changes in UV-vis absorption (a, b, and c, respectively) and luminescence (d, e, and f, respectively) spectra upon incremental addition of OH^- in dimethylsulfoxide for **1**, **2**, and **3**, respectively.

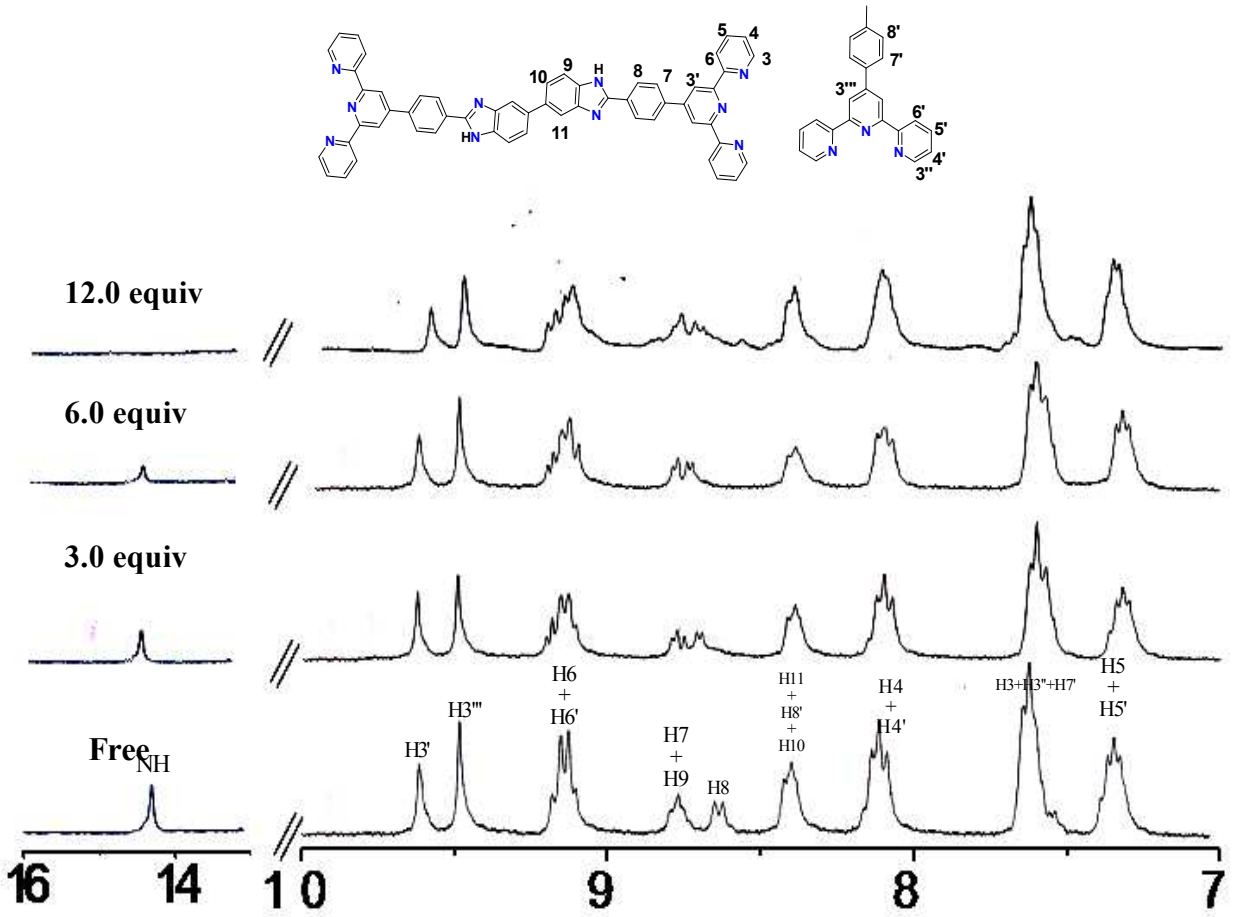

Figure S65. ^{1}H NMR titration of **1** in DMSO-d_6 solution upon incremental addition of F^- ion (0-12.0 equiv).

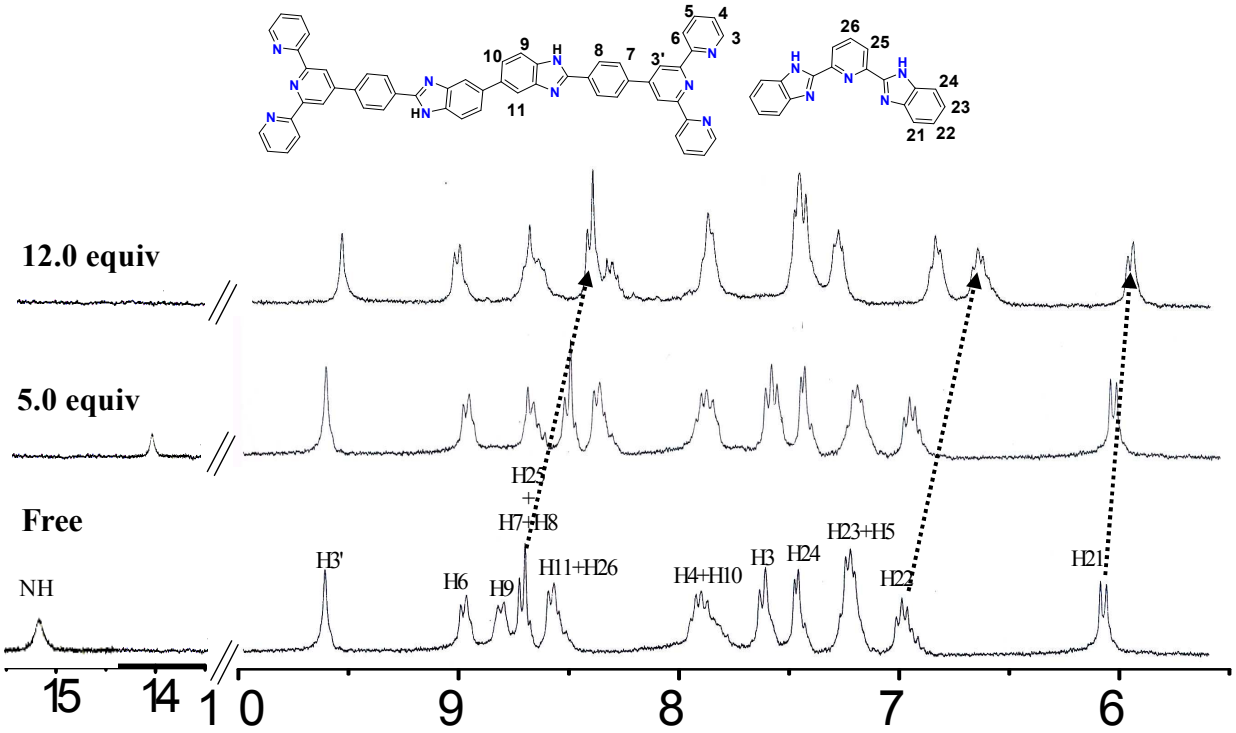

Figure S66. ^{1}H NMR titration of **3** in DMSO-d_6 solution upon incremental addition of F^- ion (0-12.0 equiv).

References

S1. Frisch, M. J.; Trucks, G. W.; Schlegel, H. B.; Scuseria, G. E.; Robb, M. A.; Cheeseman, J. R.; Scalmani, G.; Barone, V.; Mennucci, B.; Petersson, G. A.; Nakatsuji, H.; Caricato, M.; Li, X.; Hratchian, H. P.; Izmaylov, A. F.; Bloino, J.; Zheng, G.; Sonnenberg, J. L.; Hada, M.; Ehara, M.; Toyota, K.; Fukuda, R.; Hasegawa, J.; Ishida, M.; Nakajima, T.; Honda, Y.; Kitao, O.; Nakai, H.; Vreven, T.; Jr. Montgomery, J. A., Peralta, J. E.; Ogliaro, F.; Bearpark, M.; Heyd, J. J.; Brothers, E.; Kudin, K. N.; Staroverov, V. N.; Kobayashi, R.; Normand, J.; Raghavachari, Rendell, K. A.; Burant, J. C.; Iyengar, S. S.; Tomasi, J.; Cossi, M.; Rega, N.; Millam, J. M.; Klene, M.; Knox, J. E.; Cross, J. B.; Bakken, V.; Adamo, C.; Jaramillo, J.; Gomperts, R.; Stratmann, R. E.; Yazyev, O.; Austin, A. J.; Cammi, R.; Pomelli, C.; Ochterski, J. W.; Martin, R. L.; Morokuma, K.; Zakrzewski, V. G.; Voth, G. A.; Salvador, P.; Dannenberg, J. J.; Dapprich, S.; Daniels, A. D.; Farkas, Ö.; Foresman, J. B.; Ortiz, J. V.; Cioslowski, J.; Fox, D. J. Gaussian 09, revision A.02; Gaussian Inc.: Wallingford, CT, **2009**.

S2. Becke, A. D. Densityfunctional thermochemistry. III. The role of exact exchange. *J. Chem. Phys.* **1993**, *98,* 5648-5652.

S3. Lee, C. T.; Yang, W. T.; Parr, R. G. Development of the Colle-Salvetti correlation-energy formula into a functional of the electron density. *Phys. Rev. B* **1988**, *37*, 785-789.

S4. (a) Andrae, D.; Haeussermann, U.; Dolg, M.; Stoll, H.; Preuss, H. Energy-adjusted*ab initio* pseudopotentials for the second and third row transition elements. *Theor. Chim. Acta.* **1990**, *77*, 123-141. (b) Fuentealba, P.; Preuss, H.; Stoll, H.; Szentpaly, L. V. A proper account of core-polarization with pseudopotentials: single valence-electron alkali compounds. *Chem. Phys. Lett*. **1989**, *89*, 418-422.

S5. Hay, P. J.; Wadt, W. R. *Ab initio* effective core potentials for molecular calculations. Potentials for K to Au including the outermost core orbitals. *J. Chem. Phys.* **1985**, *82*, 299-310.

S6. Casida, M. E.; Jamorski, C.; Casida, K. C.; Salahub, D. R. Molecular excitation energy to high-lying bound state from time-dependent density functional response theory: charecterization and correction of the time dependent local density approximation ionization thresold. *J. Chem. Phys.* **1998**, *108*, 4439-4449.

S7. Stratmann, R. E.; Scuseria, G. E.; Frisch, M. J. An efficient implementation of time-dependent density-functional theory for the calculation of excitation energies of large molecules. *J. Chem. Phys.* **1998**, *109*, 8218-8224.

S8. Walters, V. A.; Hadad, C. M.; Thiel, Y.; Colson, S. D.; Wiberg, K. B.; Johnson, P. M.; Foresman, J. B. Assignment of the A State in Bicyclobutane. The Multiphoton ionization spectrum and calculations of transition energies *J. Am. Chem. Soc.* **1991**, *113*, 4782-4791.

S9. (a) Tomasi, J.; Mennucci, B.; Cammi, R. Quantum Mechanical Continuum Solvation Models. *Chem. Rev*. **2005**, *105*, 2999-3094. (b) Cossi, M.; Scalmani, G.; Rega, N.; Barone, V. New developments in the polarizable continuum model for quantum mechanical and classical calculations on molecules in solution. *J. Chem. Phys*. **2002**, *117*, 43-54.

S10. Caricato, M.; Mennucci, B.; Tomasi, J.; Ingrosso, F.; Cammi, R.; Corni, S.; Scalmani, G. Formation and relaxation of excited states in solution: a new time dependent polarizable continuum model based on time dependent density functional theory. *J. Chem. Phys*. **2006**, *124*, 124520-124530.

S11. Mennucci, B.; Cappelli, C.; Guido, C. A.; Cammi, R.; Tomasi, J. Structures and properties of electronically excited chromophores in solution from the polarizable continuum model coupled to the time-dependent density functional theory. *J. Phys. Chem. A* **2009**, *113*, 3009.

S12. Dennington, R. II.; Keith T.; Millam, J. *Gauss View 3*; Semichem, Inc.: Shawnee Mission, KS, **2007**.

S13. O Boyle, N. M.; Tenderholt, A. L.; Langner, K. M. cclib: A library for package-independent computational chemistry algorithms. *J. Comput. Chem*. **2008**, *29*, 839.

S14. Schneider, H.-J.; Yatsimirsky, A. *Principles and Methods in Supramolecular Chemistry*; John Wiley & Sons: England, 2000, 142.